Airbursts and Cratering Impacts

2023 | Volume 1 | Issue 1 | Pages: 1–40
DOI: 10.14293/ACI.2023.0001

Research Article

Microstructures in shocked quartz: linking nuclear airbursts and meteorite impacts

Robert E. Hermes[1], Hans-Rudolf Wenk[2], James P. Kennett[3], Ted E. Bunch[4,a], Christopher R. Moore[5,6], Malcolm A. LeCompte[7], Gunther Kletetschka[8,9], A. Victor Adedeji[10], Kurt Langworthy[11], Joshua J. Razink[11], Valerie Brogden[11], Brian van Devener[12], Jesus Paulo Perez[12], Randy Polson[12], Matt Nowell[13] and Allen West[14,*]

[1]Los Alamos National Laboratory (retired), Los Alamos, NM 87545, USA; [2]Earth and Planetary Science, University of California, Berkeley, CA 94720, USA; [3]Department of Earth Science and Marine Science Institute, University of California, Santa Barbara, CA 93106, USA; [4]Geology Program, School of Earth and Sustainability, Northern Arizona University, Flagstaff, AZ 86011, USA; [5]South Carolina Institute of Archaeology and Anthropology, University of South Carolina, Columbia, SC 29208, USA; [6]SCDNR Heritage Trust Program; Land, Water, and Conservation Division, South Carolina Department of Natural Resources, Columbia, SC 27909, USA; [7]Elizabeth City State University, Center of Excellence in Remote Sensing Education and Research, Elizabeth City, NC 27909, USA; [8]Geophysical Institute, University of Alaska, Fairbanks, AK 99775, USA; [9]Faculty of Science, Charles University, Albertov 6, Prague 12843, Czech Republic; [10]Department of Natural Sciences, Elizabeth City State University, Elizabeth City, NC 27909, USA; [11]CAMCOR, University of Oregon, 1443 E 13th Ave, Eugene, OR 97403, USA; [12]Electron Microscopy and Surface Analysis Lab, Nanofab, University of Utah, Salt Lake City, UT 84112, USA; [13]EDAX, LLC, 5794 W Las Positas Blvd, Pleasanton, CA 94588, USA; [14]Comet Research Group, Prescott, AZ 86301, USA

[a]Co-author T.E.B. passed away during the writing of this manuscript.
*Correspondence to: Allen West, E-mail: CometResearchGroup@gmail.com, allen7633@aol.com

Received: 12 August 2023; Revised: 12 August 2023; Accepted: 23 August 2023; Published online: 28 September 2023

How to cite: Hermes R.E., et al. Microstructures in shocked quartz: linking nuclear airbursts and meteorite impacts. *Airbursts and Cratering Impacts*. 2023 | Volume 1 | Issue 1 | Pages: 1–40 | DOI: 10.14293/ACI.2023.0001

ABSTRACT

Many studies of hypervelocity impact craters have described the characteristics of quartz grains shock-metamorphosed at high pressures of >10 GPa. In contrast, few studies have investigated shock metamorphism at lower shock pressures. In this study, we test the hypothesis that low-pressure shock metamorphism occurs in near-surface nuclear airbursts and that this process shares essential characteristics with crater-forming impact events. To investigate low-grade shock microstructures, we compared quartz grains from Meteor Crater, a 1.2-km-wide impact crater, to those from near-surface nuclear airbursts at the Alamogordo Bombing Range, New Mexico in 1945 and Kazakhstan in 1949/1953. This investigation utilized a comprehensive analytical suite of high-resolution techniques, including transmission electron microscopy (TEM) and electron backscatter diffraction (EBSD). Meteor Crater and the nuclear test sites all exhibit quartz grains with closely spaced, sub-micron-wide fractures that appear to have formed at low shock pressures. Significantly, these micro-fractures are closely associated with Dauphiné twins and are filled with amorphous silica (glass), widely considered a classic indicator of shock metamorphism. Thus, this study confirms that glass-filled shock fractures in quartz form during near-surface nuclear airbursts, as well as crater-forming impact events, and by extension, it suggests that they may form in any near-surface cosmic airbursts in which the shockwave is coupled to Earth's surface, as has been proposed. The robust characterization of such events is crucial because of their potential catastrophic effects on the Earth's environmental and biotic systems.

KEYWORDS

nuclear/atomic detonations, impact craters, shocked quartz, shock fractures, planar deformation features, planar fractures, tectonic deformation lamellae, electron backscatter diffraction (EBSD), transmission electron microscopy (TEM), cathodoluminescence (CL)

Abbreviations

CL: cathodoluminescence; DLs: tectonic deformation lamellae; EBSD: electron backscatter diffraction; EDS: energy-dispersive x-ray spectroscopy; EPI: epi-illumination microscopy; FFT: fast-Fourier transform; FIB: focused ion beam milling; GPa: gigapascal; OPT: optical microscopy; PDFs: planar deformation features; PFs: planar fractures; SEM: scanning electron microscopy; STEM: scanning transmission electron microscopy; TEM: transmission electron microscopy.

Introduction

In this study, we investigated quartz grains exposed to near-surface nuclear airbursts, in which the blast wave and fireball intersected the ground surface. We also compared shocked quartz grains from Arizona's Meteor Crater, a relatively small (1.2-km-wide) impact structure. Our objective was to compare quartz grains exposed to pressures and temperatures associated with these two types of high-temperature, high-pressure events. We explored the hypothesis that low-altitude nuclear airbursts marked by relatively low pressures can produce shock fractures in quartz grains filled with amorphous silica. We also investigated whether these characteristic shock fractures in quartz grains formed similarly to those during crater-forming impacts, such as at Meteor Crater. Studies of crater-forming impacts and airbursts are crucial because they potentially have sudden, radical effects on the Earth's environmental and biotic systems. However, most current studies have focused on ancient, large cratering events, such as that which occurred at the Cretaceous-Tertiary (KPg) boundary [1]. Relatively little is known about smaller, younger events, especially those caused by comets that may produce airbursts rather than large impact craters.

Previously, Eby et al. [2] and Lussier et al. [3] explored shocked quartz grains' characteristics and formation mechanism resulting from the 1945 Trinity nuclear detonation at the Alamogordo Bombing Range, New Mexico. These studies revealed the presence of linear fractures that result from the high shock pressures of these detonations, leading Lussier et al. [3] to conclude that they may represent the initial deformational feature of quartz formed in a progression of increasing shock pressures. In another investigation related to the 1945 Hiroshima nuclear detonation, Wannier et al. [4] investigated glassy spherules but found that any shocked quartz grains that may have been present in the melt had been fully amorphized due to the extremely high temperatures.

Several laboratory experiments have investigated the shock-related transformation of quartz to amorphous silica. For example, in quartz grains experimentally shocked at 5 to 17.5 GPa, Fazio et al. [5] observed glass veins composed of amorphous silica extending across several microns in length and generally thicker than 50 nm. Wilk et al. [6] found amorphous silica in experimentally shocked rocks called shatter cones that formed at low shock pressures of 0.5–5 GPa. Shatter cones are considered to be a classic impact indicator. In addition, Carl et al. [7] conducted experiments demonstrating that extensive amorphization of quartz begins at ~10 GPa. Regarding the importance of amorphous silica in studies of shock metamorphism, French and Koeberl [8] wrote, "amorphous or 'glassy' phases ... constitute another set of unique and distinctive criteria for the recognition of shock-metamorphosed rocks...." Similarly, Bohor et al. [9] wrote, "the formation of quartz glass within fractures ... allows a definitive distinction ... between these shock PDFs and the glass-free dislocation trails marking slow tectonic deformation."

Even with these pioneering investigations, numerous questions remain about the formation of shock fractures and amorphous silica associated with nuclear airbursts. Is the formation process similar to that for planar fractures (PFs) and planar deformation features (PDFs) found in shocked quartz grains associated with cosmic impact craters? Are these features similar or different from tectonic lamellae in some deformed metamorphic rocks? In this contribution, we explore these and other questions.

Shock metamorphism in quartz

Previous studies of impact structures identified relatively low shock fractures in quartz and gave them various names, including shock extension fractures (SEFs) [10–13], shock fractures [14, 15], and vermicular (i.e., wormlike) microfractures [11, 13, 16]. Here, we adopt the term "shock fractures" to denote non-planar, shock-induced microfractures in quartz. They are often filled with amorphous silica, a term we use interchangeably with "glass."

Multiple studies have reported different types of shock metamorphism observed in quartz, including planar deformation features (PDFs) [8, 9, 17–26], planar fractures (PFs) [8, 27], tectonic deformation lamellae (DLs) [8, 9, 14, 19, 21, 24, 28–31], and shock micro-fractures [26, 32–37]. Here, the term "lamellae" typically denotes parallel and planar stress features that form at high shock pressures in quartz. In contrast, the term "fractures" denotes typically open or glass-filled stress features that are sub-planar and sub-parallel. Table 1 compares some of the commonalities

Table 1: Characteristics of metamorphism of quartz.

Characteristics	Shock fractures	PDFs	PFs	DLs
Fractures rather than lamellae	Yes	No	Yes	No
Features crystallographically controlled	No	Yes	Yes	Sometimes
Multiple oriented sets of fractures/lamellae	Weakly oriented	1–6+	1–6+	1–2
Planar fractures/lamellae	Sub-planar	Planar	Planar	Sub-planar
Parallel fractures/lamellae	Sub-parallel	Parallel	Parallel	Sub-parallel
Thickness of fractures/lamellae	nm to μms	Usually ≤1 μm	Usually ≥3 μm	Usually ≥2 μm
Features filled with amorphous silica	Often	Often	Sometimes	Never
Spacing between fractures/lamellae	nm to μms	Usually <1 μm	Usually >20 μm	Usually ≥5 μm
Estimated formation pressure (Gpa)	≥3	~10–25	<10	<1
Estimated formation speed	<1 sec	<1 sec	<1 sec	Very slow
	Shared features:	**2 of 10**	**4 of 10**	**2 of 10**

Note. Shock micro-fractures investigated in this study share 2 of 10 characteristics with planar deformation features (PDFs), 4 of 10 characteristics with planar fractures (PFs), and 2 of 10 with tectonic deformation lamellae (DLs). The green shading represents features in common with shock fractures in our study. Data are primarily derived from French and Koeberl [8].

and differences among the types of shock features. Our analysis of previous studies (primarily French and Koeberl [8]) shows that shock fractures share 2 of 10 characteristics with PDFs, 4 of 10 with PFs, and 2 of 10 with DLs. Thus, shock fractures differ substantially from the other shock metamorphic features: PDFs, PFs, and DLs. The most important reported differences are that shock fractures are typically sub-planar, non-parallel, not crystallographically oriented, and form at lower shock pressures.

Key analytical studies of shock fractures

Kieffer [32] performed analyses of shocked sandstone from Meteor Crater and concluded that impact-related microfractures began to form at 5.5 GPa (Table 2, adapted from Table 2 of Kieffer [32]). Later, Kieffer et al. [33] described quartz grains within sandstone from Meteor Crater that were weakly shocked at <10 GPa and displayed fractures with quartz that was transformed into amorphous silica. For moderately and strongly shocked rocks, they proposed a process called "jetting," in which molten quartz was injected under pressure into shock-formed fractures in the grains.

Christie et al. [18] performed laboratory experiments on milled quartz cylinders by generating slow-strain conditions to produce glassy lamellae using a confining pressure of 1.5 GPa and a stress differential of up to 3.6 GPa. Their experiment attempted to replicate the features known to form in quartz grains during tectonic motion along fault planes. They reported the presence of deformation lamellae closely associated with amorphous silica at low pressures under laboratory conditions. Their experiment suggests that glass-filled lamellae may form in quartz at pressures as low as 1.5 GPa.

Importantly, Christie et al. [18] did not report amorphous silica associated with naturally-formed tectonic deformation lamellae in quartz [19], suggesting that their laboratory experiments did not replicate the processes that form natural tectonic lamellae. Co-author H.-R.W. has performed multiple analyses of tectonic lamellae and, notably, never observed amorphous silica associated with tectonic lamellae in quartz grains [40–44]. In addition, Houser et al. [45] described finding tectonically-formed, nano- to micro-scale amorphous silica particles and nanofilms along active fault planes, but they reported no quartz grains with fractures containing amorphous silica. Multiple studies have observed amorphous silica within fractures, but only in impact-related shocked quartz and not in tectonic deformation lamellae [9, 14, 19].

Laboratory experiments by Kowitz et al. [11, 15, 46] investigated the shock alteration of quartz grains when a

Table 2: Classification of shock stages for quartz.

Shock stage	Range, low (GPa)	Range, high (GPa)	Lithology
0	≤0.2	0.9	Undeformed, porous sandstone
1a	0.9	3	Compacted, porous, deformed sandstone
1b	3	5.5	Compacted, non-porous, deformed sandstone
2	5.5	13	Dense sandstone with 3 to 10 wt% glass and <95% quartz
3	13	39	Dense sandstone with up to 20 wt% glass and 45 to 80 wt% quartz
4	>30	–	Dense sandstone with 20 to 75 wt% glass and 15 to 45 wt% quartz
5	–	–	Vesicular rock with 80 to 100 wt% glass and up to 15% quartz

Note. Based on a study of quartz-rich sandstone from Meteor Crater [32, 33]. The scale ranges from unshocked quartz at shock stage 0 to highly shocked quartz at shock stage 4 and melted quartz glass at shock stage 5. Shock-generated fractures with amorphous silica (glass) first appear at ~5.0 to 5.5 GPa, as green highlighting indicates. This classification is from Kowitz et al. [11], based on Table 2 of Kieffer [32, 33] and modified by others [38, 39].

steel plate was explosively driven into cylinders of quartz-rich sandstone at pressures of ~5, 7.5, 10, and 12.5 GPa (Figure 1). Visible shock fractures and amorphous silica (~1.6 wt%) first appeared at ~5 GPa [11]. Scanning electron microscopy (SEM) images reveal shock fractures called "sub-planar, intra-granular fractures [11]." This result is significant because most shocked material within small impact craters forms within this lower shock pressure range. The combined shock effects from studies by Kieffer [32, 33] and Kowitz et al. [11, 15, 46] are summarized in Table 2.

The Trinity nuclear airburst has been recently estimated at 24.8 ± 2 kiloton (kt), up from previous estimates of 20–22 kt. The presence of various key minerals is indicative of the extreme pressures generated: ~8 to < 10 GPa for shocked quartz [2, 3]; ~7–10 GPa for shocked zircon [47]; <25–60 GPa for vesiculated feldspar [48]; >8 GPa based on the fractionation of zinc [49]; and 5–8 GPa based on quasi-crystalline minerals in trinitite [50]. These studies of the Trinity airburst are critical because they establish the high pressures typically necessary for producing shock metamorphism.

Sample locations

Meteor Crater, Arizona

This site, also known as the Barringer Crater, is a 1.2-km-wide hypervelocity impact feature located east of Flagstaff, Arizona [51]. The 180-m-deep crater is surrounded by an ejecta blanket that is elevated ~30 to 60 m above the local surface (Figure 2). The 50,000-year-old impact crater is estimated to have been produced by an approximately 50-m-wide bolide, now known as the Canyon Diablo meteorite [51]. The bedrock inside Meteor Crater contains shocked quartz with high-pressure planar deformation features (PDFs) [32, 51], but we limited our study to shock-fractured quartz grains embedded in samples of meltglass that had been ejected from the crater; we did not examine quartz grains embedded in sandstone or limestone (Appendix, Figure S1). The samples were collected in 1966 by Bunch [51] on the rim ~500 m north of the crater's center at ~35.032206° N, 111.023988° W.

Russia, Joe-1 and Joe-4 nuclear tests, near-surface airbursts

The first Soviet nuclear bomb test, nicknamed "Joe 1" by the Americans, was conducted in 1949 in Kazakhstan (~50.590664°

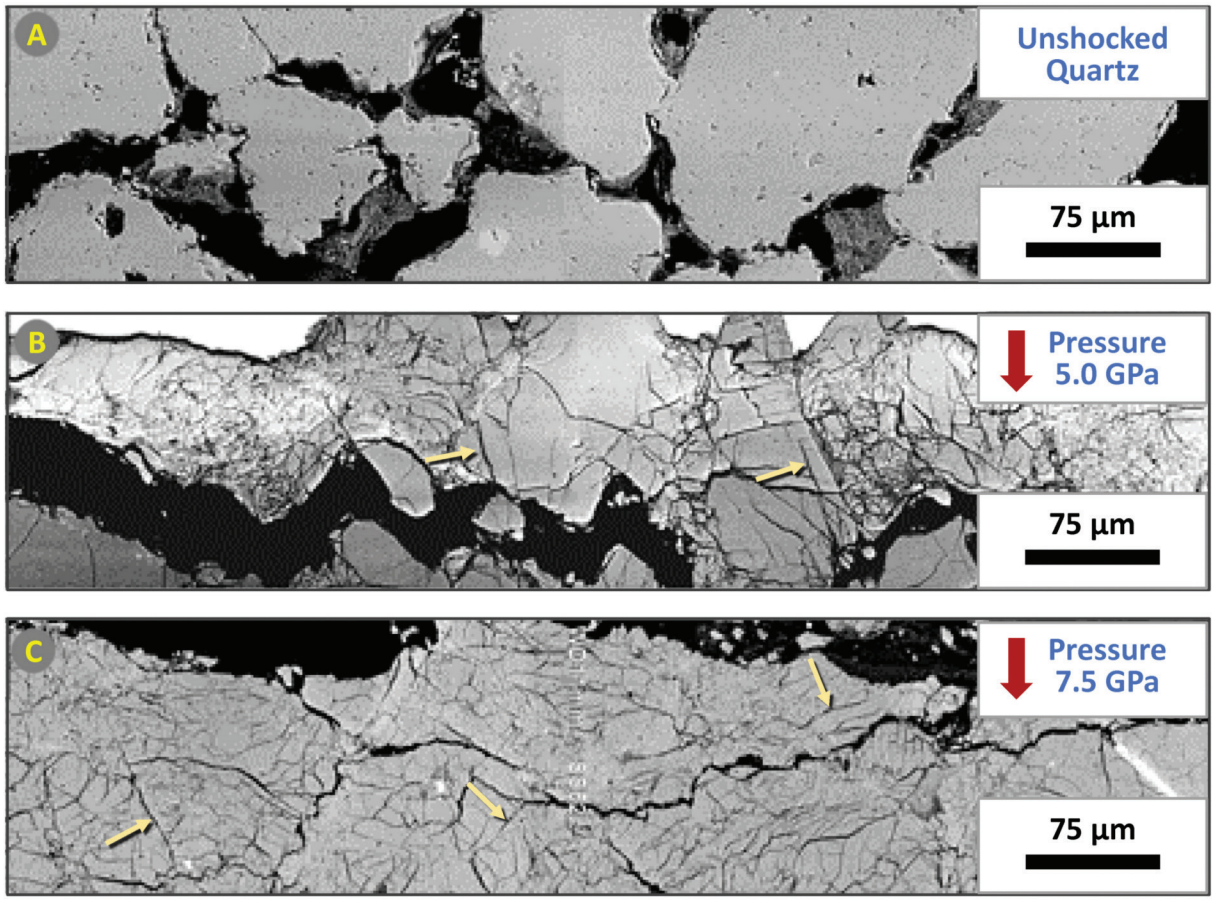

Figure 1: Low-shock fractures in quartz. SEM backscatter electron (BSE) images of polished, thin-sectioned grains from shock experiments by Kowitz et al. [11] showing **(A)** original unshocked quartz grains in porous sandstone; **(B)** grains with non-planar, intra-granular microfractures initially produced at 5 GPa; **(C)** grains shocked at 7.5 GPa. Red arrows mark the direction of the applied shock from the top of the images down; yellow arrows mark selected representative fractures. Adapted and cropped from Kowitz et al. [11]; used with permission.

Figure 2: Meteor Crater, Arizona. 1.2-km-wide impact crater near Flagstaff in northern Arizona [51]. The 180-m-deep crater is surrounded by an ejecta blanket elevated ~30 to 60 m above the plateau. Source: "Meteor Crater" 35.032206° N, 111.023988° W. Google Earth. Imagery date: 2022. Yellow pin marks the location of sample analyzed. Accessed: 10/08/2022. Permissions: https://about.google/brand-resource-center/products-and-services/geo-guidelines/.

N, 77.847319° E). The ~20-kt nuclear test was detonated aerially on a 30-m-tall tower (Figure 3). "Joe 4" is the American nickname for a 400-kt Russian test that was detonated on a 30-m-tall tower at the same location in 1953. This study analyzed only fractured quartz grains in loose sediment and embedded in multi-mm-sized fragments of meltglass. A surface sediment sample was collected by Byron Ristvet on 9/1/2012 at ~100 meters from ground zero for both tests (Appendix, Figure S2). It could not be determined which nuclear test produced the sample that was collected and investigated.

U.S., Trinity nuclear test, near-surface airburst

The Trinity nuclear bomb was detonated aerially in 1945 at the Alamogordo Bombing Range, New Mexico, on a tower at an altitude of 30 m [2] with an estimated energy of 24.8 kilotons (kt) of TNT equivalent [52]. The fireball was ~300 m wide at ~25 ms after detonation (Figure 4A). A blast zone of the ejected materials extended more than 400 m radially from ground zero [2]. The airburst formed a crater that was ~80 m in diameter [53] and ~1.4 m deep [54] (Figure 4B). This study analyzed only fractured quartz grains embedded in meltglass, called trinitite, which was collected by co-author R.E.H. on 9/30/2011 from the ground surface ~400 m north of ground zero (33.68100° N, 106.4756° W) (Appendix, Figure S3). R.E.H. also studied another sample (JIE) of loose quartz grains found on an anthill near ground zero, collected by Jim Eckles in 2003.

Sampling and methodology

Samples were collected as described in the Appendix, Methods-Samples. Candidate grains were processed as described in the Appendix, Methods-Processing Steps. The Appendix also lists the locations of laboratories where analyses were performed. Selected grains were investigated using multiple standard analytical techniques and preparation methods, as described in Methods below and the Appendix, Methods-Analytical Techniques.

Results and discussion

We employed ten analytical techniques to investigate shock fractures containing amorphous silica, as follows:

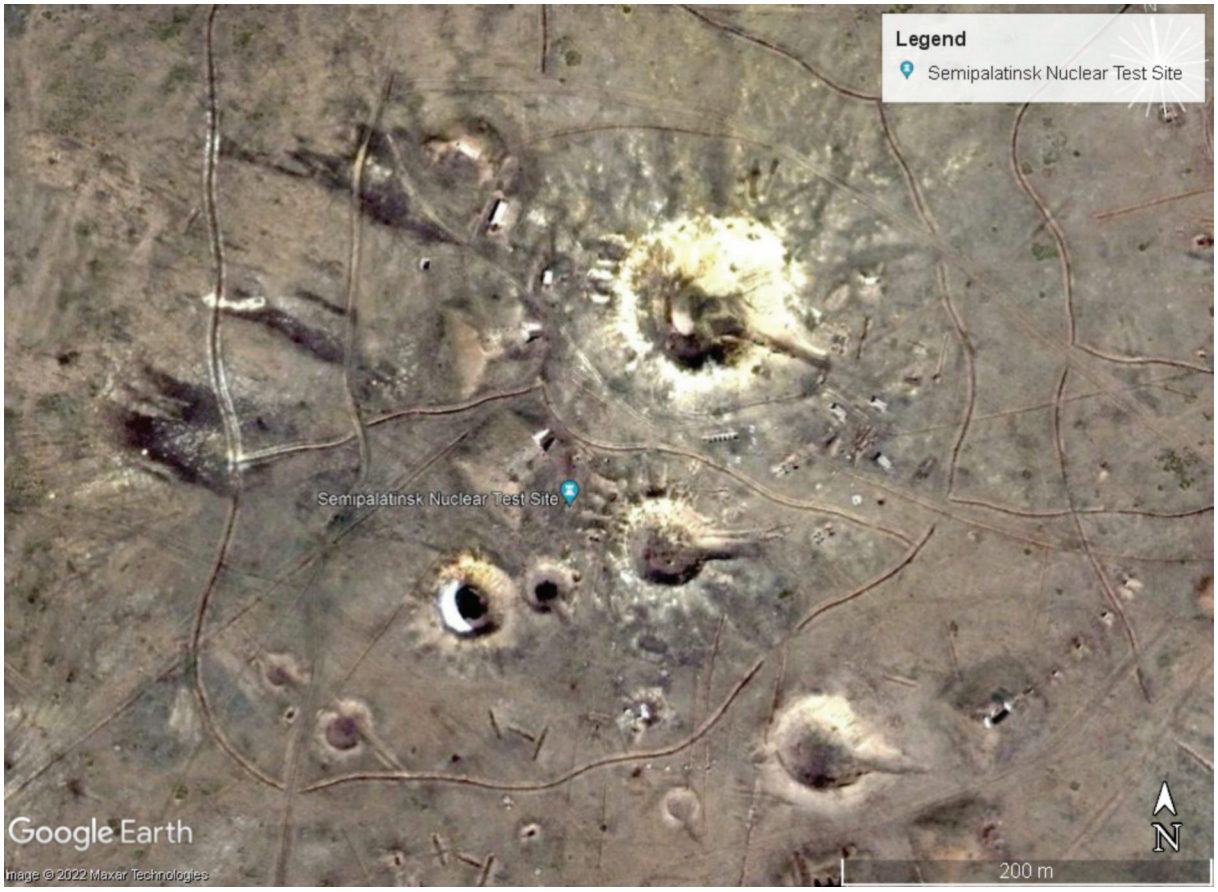

Figure 3: Semipalatinsk Nuclear Test Site, Kazakhstan. Photo of the general area for the detonations of Joe-1 and Joe-4 and other nuclear bomb craters. Source of base image: "Joe-1 test" 50.590664° N, 77.847319° E. Google Earth; Maxar Technologies. Imagery date: 2022. Accessed: 10/08/2022. Permissions: https://about.google/brand-resource-center/products-and-services/geo-guidelines/.

Optical transmission microscopy (OPT)

Using this technique, we observed that >50% of the grains examined for each of the three sites displayed shock fractures. Representative optical and SEM-BSE images of quartz grains are shown in Figure 5. These images are comparable to those from the experimental study shown in Figure 1. Most displayed a single set of shock fractures, meaning all are oriented in approximately the same direction. However, a few grains display multiple sets oriented along different axes.

Some grains with shock fractures display undulose extinction (Figure 5), in which waves of extinction are typically oriented perpendicular to the trend of the grain's lamellae. Kowitz et al. [15] reported that the extinction of quartz grains is sharp in unshocked sandstone. In contrast, they noted that undulose extinction becomes apparent in sandstone shocked to 5 GPa, transitioning to weak but still prominent mosaicism (i.e., irregular patchwork extinction) (Figure 5).

Epi-illumination microscopy (EPI)

This analytical technique is particularly useful in viewing HF-etched quartz grains (Figure 5) that display previously hidden glass-filled fractures. Multiple studies [9, 14, 19, 21, 55, 56] have demonstrated the usefulness of performing analyses after etching quartz grains with HF. According to Gratz et al. [19], the HF-etching removes some amorphous silica filling the shock features, allowing for the "unambiguous visual distinction between glass-filled PDFs and glass-free tectonic deformation arrays in quartz." Other techniques are necessary to identify and characterize the filled material as amorphous silica, a key indicator of shock metamorphism [9, 19].

In contrast, lamellae in tectonically-deformed grains are not visible in EPI as open fractures but may appear as shallow, closed depressions without filling material. Our investigations of six unshocked natural quartz grains and six tectonically-deformed quartz grains from non-impact layers reveal that none contain amorphous silica. See Figure 15 and 16.

Scanning electron microscopy (SEM-BSE)

Analyses using SEM-BSE revealed filled fractures in quartz grains that appeared mostly as linear features, although some were curvilinear. Other analyses are also necessary to identify and characterize the material filling the fractures.

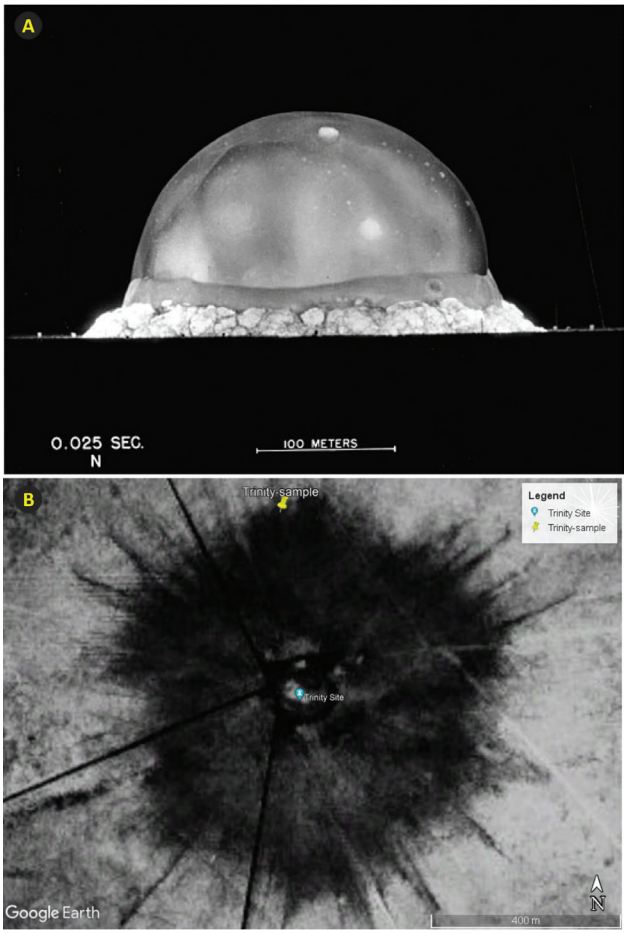

Figure 4: Trinity Test Site in New Mexico. (A) Trinity ~300-meter-wide nuclear fireball, taken 25 ms after 24.8-kt detonation. Photo date: July 16, 1945. Courtesy of US Govt. Defense Threat Reduction Agency. Source: http://www.nuclearchive.com/Photos/Trinity/image8.shtml. This work is in the public domain. **(B)** Post-detonation photograph. The photo was taken in July 1945, approximately 28 hours after the blast. The dark color represents trinitite glass within a ~400-meter-radius blast zone, which was discontinuously covered with ejected dark trinitite glass. Note that dark streaks of material radiate from ground zero. Source: "Trinity," 33.68100° N, 106.4756° W. Google Earth. Imagery accessed: 10/08/2022. Permissions: https://about.google/brand-resource-center/products-and-services/geo-guidelines/.

Scanning transmission electron microscopy (STEM)

FIB locations of analyzed grains are shown in Figure 5. Using dark-field STEM, the 8- to 15-µm-wide foils display inter-fracture spacings ranging from ~250 nm to 3 µm (Figure 6). Nearly all shock fractures were observed to contain material that was shown to be amorphous silica discontinuously filling the fractures.

Transmission electron microscopy (TEM)

Images acquired using bright-field TEM show sub-planar shock fractures containing thin bands of amorphous silica (Figure 6). We confirmed the amorphous state of the fill material using high-resolution bright-field TEM that can image individual atoms (Figure 7).

Numerous inclusions, also known as decorations or vesicles, are filled with glass or gases and are closely associated with shock fractures (Figure 6). Madden et al. [57] reported that multi-phase inclusions of glass, gases, and fluids are typical at Meteor Crater in sandstone lightly shocked at ≥5.5 to 13 GPa. In contrast, that study observed no multi-phase inclusions in samples formed at >13 GPa in shock stages 3 or 4, suggesting that the high shock pressures collapsed the inclusions [57]. Thus, the evidence suggests that these grains with shock fractures formed at low pressure of 5 to 13 GPa at shock stages 1 to 2. In contrast, unshocked tectonically-deformed quartz grains may display lines of bubbles, known as decorations, that form by the dissolution of quartz by water rather than by shock-related processes.

Fast-Fourier transform (FFT)

The areas of the grains from which the foils were extracted are shown in Figure 5. In this study, the FFT analyses commonly displayed crystalline structure in the quartz matrix away from the shock fractures, but most shock fractures displayed a diffuse halo or ring indicative of amorphous material [33, 58, 59], especially in the thin bands of glass along the shock fractures (Figures 6 and 7).

FFTs of the filling along these thin fractures display the diffuse halo-like patterns characteristic of amorphous material [33, 58, 59]. The halos have average d-spacings of ~3.72 Å for Meteor Crater, ~3.90 Å for Joe-1/4, and ~3.95 Å for Trinity (Figure 6). Other average halo d-spacings are shown in Figure 7. The mean value of 10 grains for the three sites is 3.60 Å with a range of 3.34 to 3.95 Å. Plots show typical halo d-spacings for each of the three sites that are somewhat lower than the reported halo d-spacing of 4.2 Å for quartz glass [60] (Figure 8).

Gleason et al. [61] conducted experiments on amorphous silica and noted that unshocked amorphous silica had a d-spacing of about 4.20 Å. In contrast, shock pressures ranging from 4.7 to 33.6 GPa transformed the quartz into amorphous silica that was permanently densified, causing the standard glass d-spacing to decrease within a range of 3.36 to 4.00 Å. Thus, in our study, the lower d-spacing values (mean = 3.62 Å) support an interpretation that amorphous silica from the three sites was shocked and densified at as low as 4.7 GPa.

TEM energy dispersive spectroscopy (TEM-EDS)

Energy-dispersive X-ray spectroscopy (EDS) is an analytical technique used to determine the elemental composition of materials. EDS analyses of multiple grains demonstrated that most of the material filling fractures is predominantly composed of silicon and oxygen (range: 98–99 wt%). Together with the diffuse rings exhibited in the FFT results (Figures 6–8), this finding confirms that the material filling

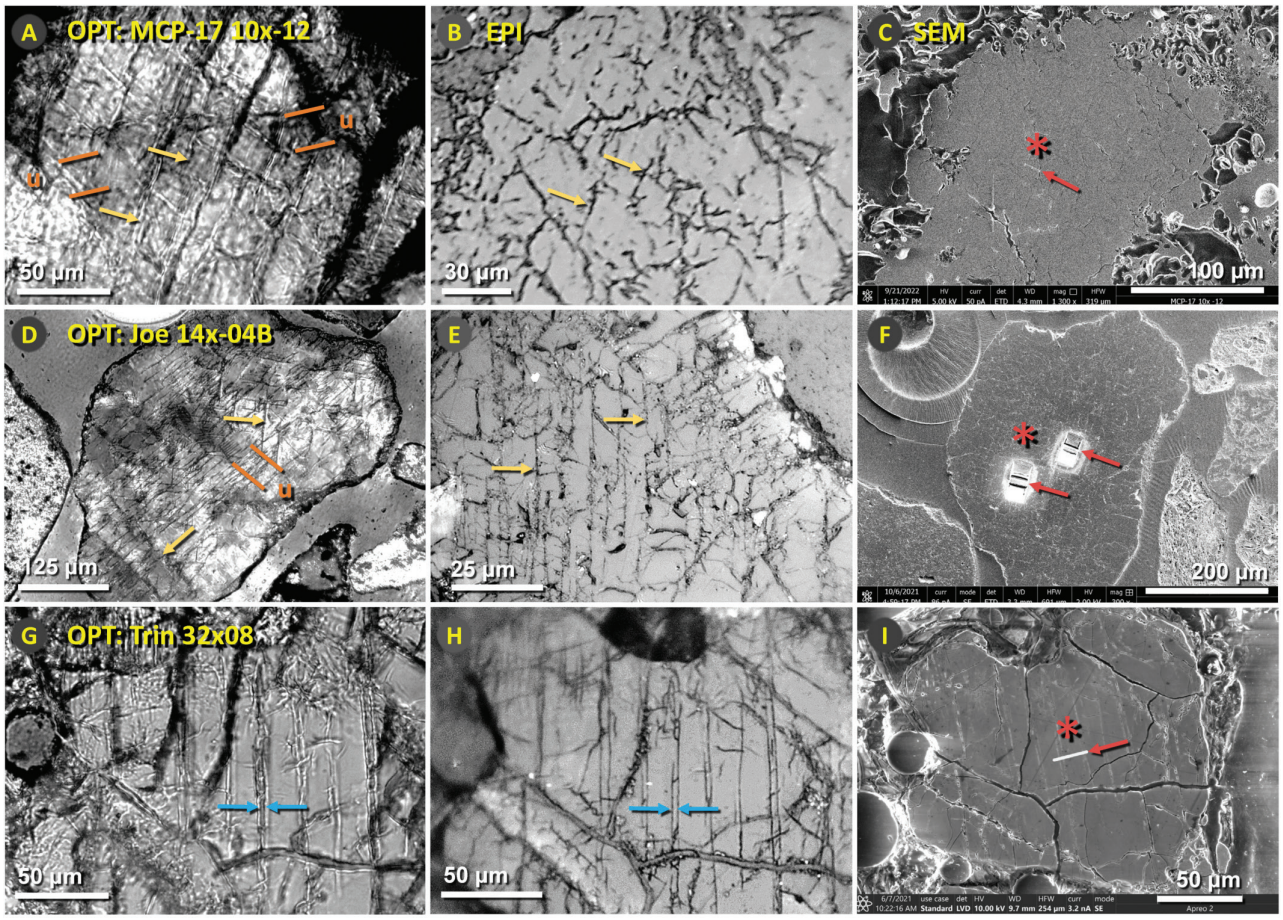

Figure 5: **Images of fractures in quartz grains**. Optical microscopy (OPT), left-hand panels **A, D, G**. Epi-illumination (EPI), middle panels **B, E, H**. Scanning electron microscopy (SEM-BSE), right-hand panels **C, F, I**. **(A-C)** Grains from Meteor Crater, Arizona. **(D-F)** Grains from the Russian Joe-1/4 nuclear test. **(G-I)** Grains from the Trinity nuclear test site. Optical images (left-hand column) were acquired under crossed polarizers rotated ~20° off maximum for better visibility. Yellow arrows indicate random representative shock fractures. Panels **A** and **D** show dark bands of undulose extinction between orange lines labeled "u." The Trinity grain in panels **G** and **H** displays oriented pairs of shock fractures between blue arrows. Red arrows in panels **C, F**, and **I** (right-hand column) mark sites from which micron-sized slices of the quartz grain were removed using the focused ion beam (FIB) and then analyzed using bright-field TEM and TEM-EDS. The red asterisks in the right-hand column mark the locations of CL and SEM-EDS analyses.

the fractures is amorphous silica. On the other hand, this Si-rich material is inconsistent with being hydrated silica (opal, hyalite) that can precipitate into fractures because the filling lacks spherical micro-structures typically present in opal [62]. Furthermore, TEM-EDS analyses reveal insufficient levels of oxygen to account for the hydration of silica (opal, hyalite) [62]. Concentrations typically total ~66 wt% oxygen in opal and hyalite [62], compared with ~28 to 48 wt% for the glass in our samples. For EDS spectra and other details, see Appendix, Figures S4–S7.

Most material that fills the fractures is amorphous silica, but some fractures are intermittently filled with C, Al, Mg, Fe, or Ca. These represent secondary materials possibly injected into the fractures during their formation, precipitated later into the fractures, or introduced during the preparation and polishing of samples.

Cathodoluminescence (CL)

The areas of grains analyzed for CL are shown in Figure 5. Representative CL images are shown in Figures 9–11. Under CL, fractures filled with amorphous silica have been reported to be commonly non-luminescent, i.e., black [21, 59, 63], although some defect structures in amorphous silica have been reported to luminesce red [65]. Alternately, open fractures also appear black; therefore, TEM and TEM-EDS must be used to confirm the possible presence or absence of amorphous silica. According to previous studies [21, 59, 63, 64], if quartz luminesces red, it has been heated or melted and then recrystallized but does not contain amorphous silica. In addition, tectonic deformation lamellae may appear red but not black [21, 59, 63, 64]. Non-shocked quartz lattice often luminesces blue under CL [21, 59, 63, 64].

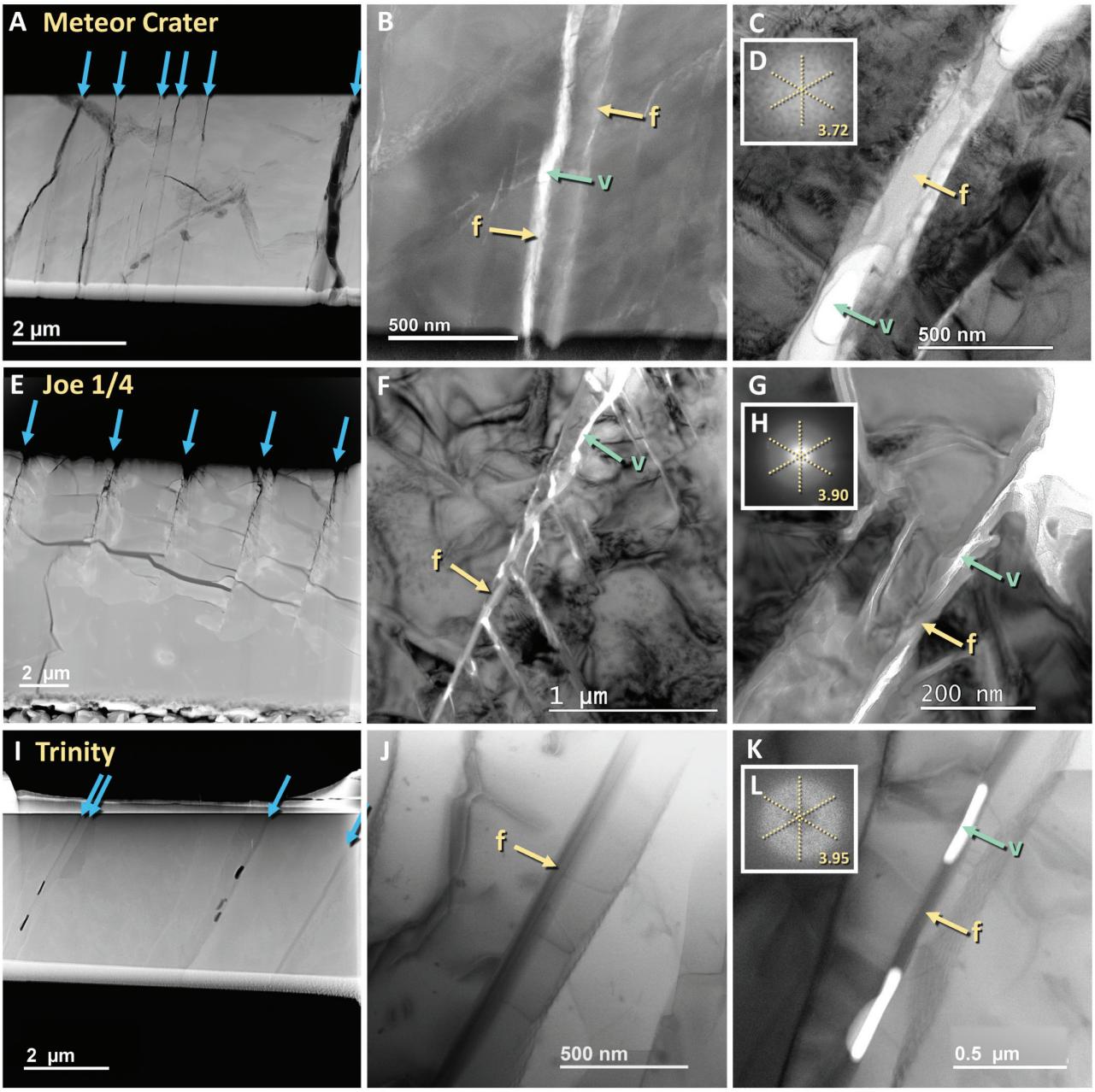

Figure 6: **Images using STEM, TEM, and fast-Fourier transform (FFT).** **(A-D)** Grain #10x-12 from Meteor Crater, Arizona. **(E-H)** Grain #14x-04 from the Russian Joe-1/4 nuclear test. **(I-L)** Grain #09x11 from Trinity meltglass. The blue arrows mark shock fractures (left-hand column) in these dark-field STEM images, in which the dark lines represent fractures, and the black areas represent voids. For bright-field TEM analyses (**middle** and **right-hand columns**), arrows labeled "f" mark material that discontinuously fills the shock fractures. Green arrows labeled "v" indicate voids that appear white in bright-field TEM mode rather than black as in dark-field STEM. Panels **D, H,** and **L** are FFTs. The diffuse halo and the d-spacings of its outer edge indicate that the filling of the fractures is amorphous silica. Halo d-spacings were measured along dashed yellow lines and averaged 3.72 Å in panel **D**, 3.90 Å in panel **H**, and 3.95 Å in panel **L**. The diameter of the bright-field TEM beam spot was ~0.5 µm. Insets of diffraction spectra were acquired at "f" in each corresponding bright-field TEM image.

SEM energy dispersive spectroscopy (SEM-EDS)

For these analyses, we selected multiple areas that displayed fractures filled with material (Figures 7 and 8). In most cases, EDS analyses indicated the quartz matrix and filling material were predominantly silica and oxygen (range: 89–98 wt%). The balance was made up of carbon, presumably from the mounting epoxy or the carbon coating. For EDS spectra and other details, see Appendix, Figures S8–S12.

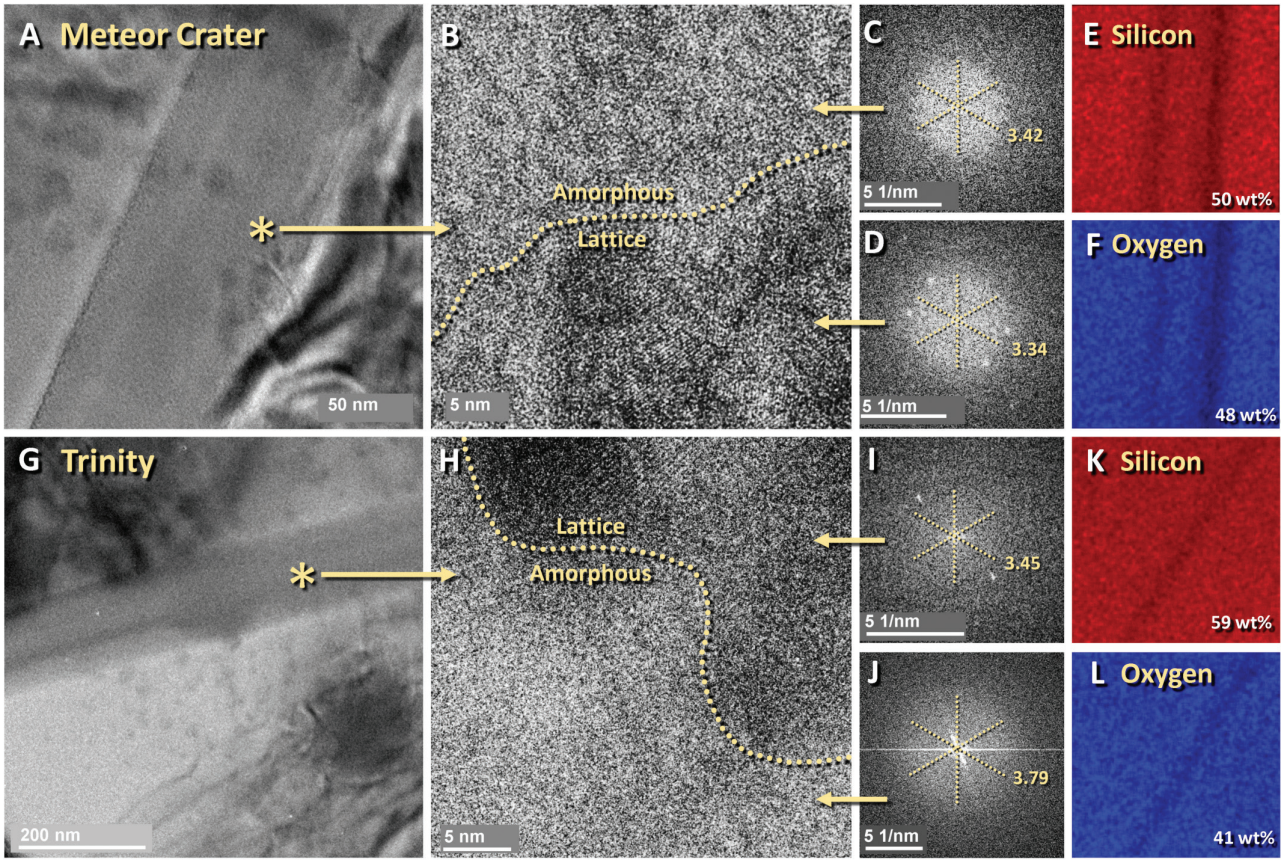

Figure 7: TEM images of quartz shock fractures filled with amorphous silica. **(A-F)** is from Meteor Crater (grain #09x-11); **(G-L)** is from Trinity (grain #09x11). **(A)** Bright-field TEM image of the region of interest. **(B)** A close-up bright-field TEM image exhibits the crystalline lattice below the dotted line and the amorphous silica above; the image was acquired at the asterisk in panel **A**. **(C)** Fast-Fourier transform (FFT) of the top part of panel **B** exhibits a diffuse halo indicative of amorphous silica with a d-spacing of 3.42 Å. **(D)** FFT of the bottom part of panel **B** exhibits diffraction spots with a halo indicative of a mix of crystalline lattice with amorphous silica. The halo measures 3.34 Å. **(E-F)** EDS panels show a composition of 98 wt% silica; the EDS spectra were acquired at the location of the asterisk in panel **A**. **(G)** Bright-field TEM image of the region of interest. **(H)** A close-up bright-field image exhibits the crystalline lattice above the dotted line and the amorphous silica below the line; the high-resolution TEM (HRTEM) image was acquired at the location of the asterisk in panel **G**. **(I)** FFT of the top part of panel **H** shows diffraction spots with a halo that measures 3.45 Å. **(J)** FFT of the bottom part of panel **H** displays a diffuse halo indicative of amorphous silica. The d-spacing of the amorphous halo is 3.79 Å. **(K-L)** EDS panels show a composition of 100 wt% silica; analyses were acquired at the location of the asterisk in panel **G**.

Electron backscatter diffraction (EBSD)

Analyses performed using EBSD rely on varying comparisons of the Kikuchi patterns in a given grain, as shown in Appendix, Figures S13–S16. Multiple EBSD routines reveal an extensive network of oriented shock fractures for all three sites (Figure 12). Optical microscopy revealed that most of the hundreds of quartz grains in each sample from the three sites display these fractures. These images closely match those from shock experiments at ≥5.5 GPa by Kowitz et al. [11] (Figure 1).

Each grain's crystallographic orientation is indicated for each image in the **left-hand column** by the crystal representation in the lower right-hand corner (Figures 12A, 12C, and 12E). The red-colored plane represents (0001), the basal plane, with the *c*-axis perpendicular. Although the shock fractures are non-planar, their general orientations correspond well with the crystallographic planes depicted on the crystal representation in the lower right-hand corner. This correspondence suggests that the shock fractures form similarly to high-shock planar deformation features (PDFs) and planar fractures (PFs) but are unlike tectonically-deformed lamellae [8, 66].

EBSD "local orientation spread" (LOS)

The high pressures during shock metamorphism damage and distort the crystalline lattice of quartz grains. To identify and quantify any potential grain damage, we used an EBSD routine called "local orientation spread" that generates Kikuchi patterns of the quartz lattice. The EDAX EBSD software compares these short-range patterns to reveal possible rotations

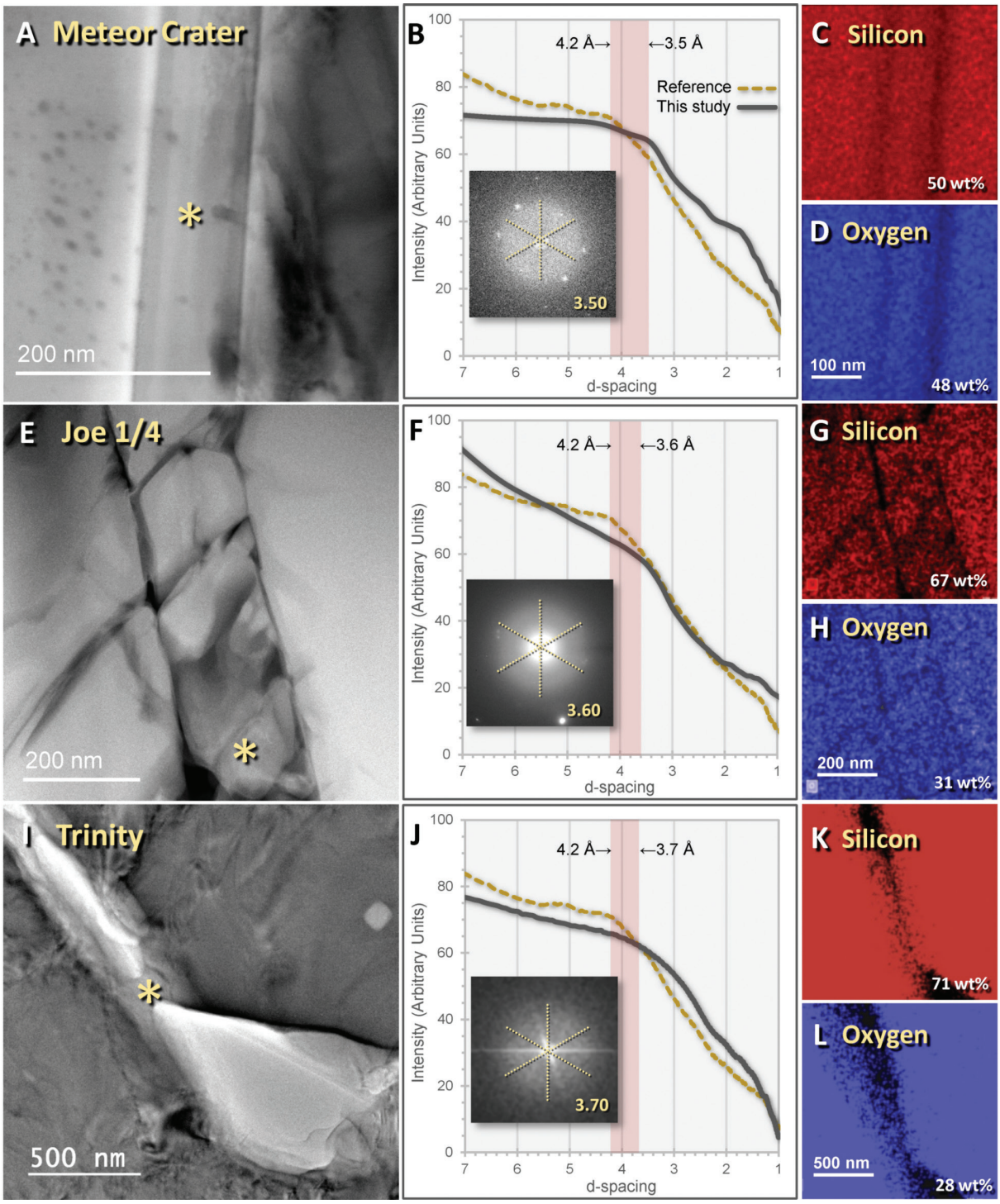

Figure 8: TEM images; FFT patterns and plots; EDS elemental maps. All images were acquired from FIB foils. **(A-D)** Grain #10x-12 from Meteor Crater, Arizona. **(E-H)** Grain #14x-04 from the Russian Joe-1/4 nuclear test. **(I-L)** Grain #30x08 from the Trinity JIE sediment sample. Bright-field TEM images (left-hand column) show the micron-sized areas analyzed; asterisks mark the locations used to generate the FFTs (middle column insets) and the EDS analyses (right-hand column). Panel **I** (Trinity) shows a glass-filled shock fracture intersecting a glass-filled vesicle. In the middle column, the graphs show intensities plotted against d-spacings generated from FFTs using the Profile function of Digital Micrograph, version 3.32.2403.0. Each grain in this study shows a decrease in slope at d-spacings ranging from 3.50 to 3.70 Å (black line), marking the edges of the diffuse halos shown in the FFT insets. The yellow dashed lines plot a reference profile of non-shocked amorphous silica (melted quartz) [60] with a slope change at 4.20 Å. The slopes of the yellow and black lines are similar, consistent with the presence of amorphous silica in the grains in this study. EDS analyses in right-hand panels confirm that the areas centered on the asterisks in the left-hand panels are predominantly silica and oxygen (range: 98–99 wt%).

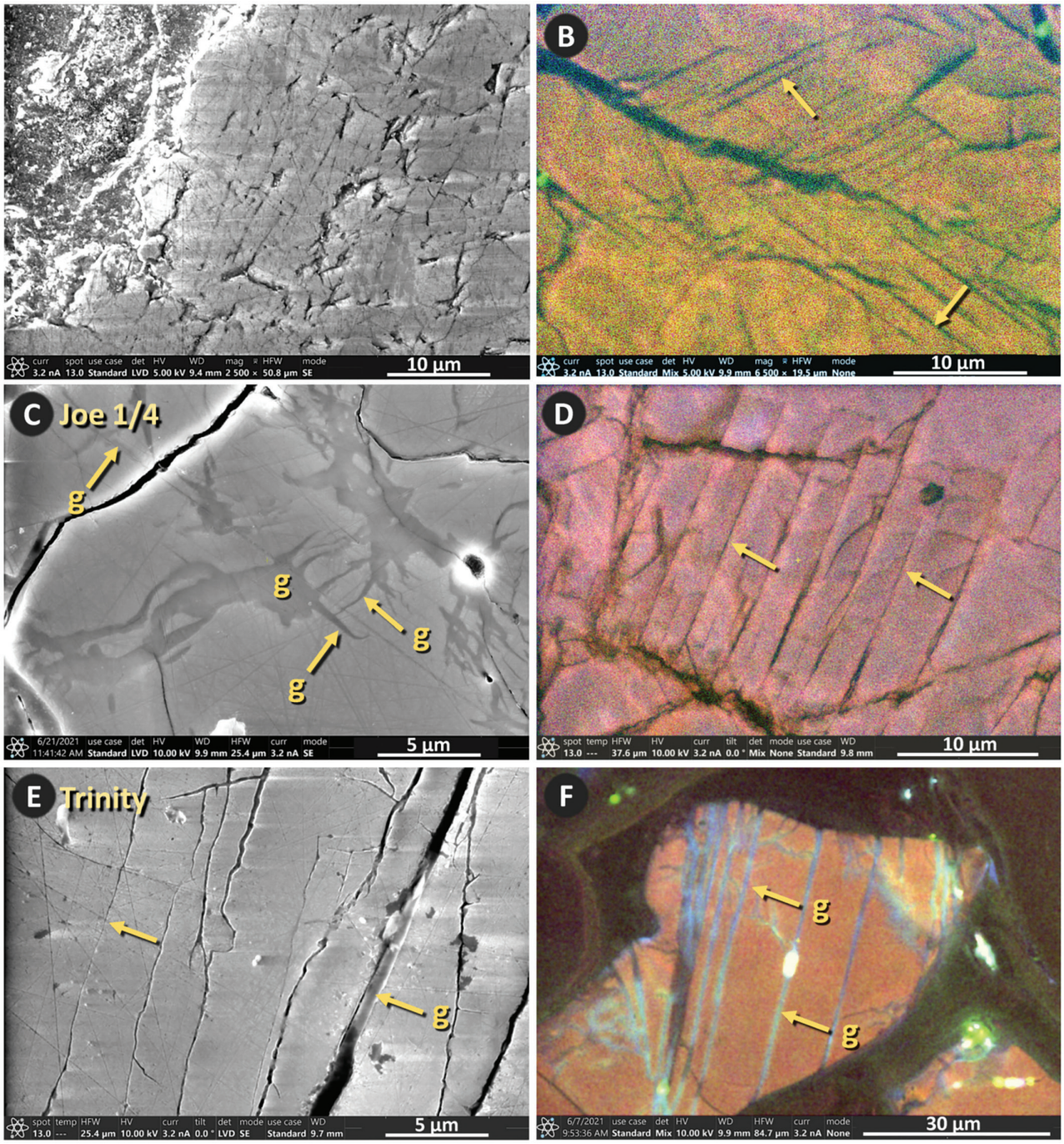

Figure 9: SEM (A-C) images and cathodoluminescence (CL) images (D-F) of shock fractures in quartz grains. **(A)** SEM-BSE image of quartz from Meteor Crater, grain 11x08. Shock fractures at arrows. **(B)** CL image of a different Meteor Crater grain 13x11 showing small, feather-like fractures angling away from the large irregular shock fracture. **(C)** SEM-BSE image from the Joe-1/4 site, grain 03x16. Most shock fractures contain darker-contrast glass (g) along the shock fractures. The web-like structure is consistent with the high-pressure injection of molten silica or *in situ* melting. **(D)** CL image of a different grain from the Joe-1/4 site, grain 14x-04b. **(E)** SEM-BSE image of quartz from the Trinity site, grain 09x11. The arrow at "g" marks non-luminescent glass. **(F)** CL image of a different grain, 06x14, from Trinity meltglass. Note that shock fractures are filled with bluish-gray-to-black, non-luminescent glass.

or misorientations of the crystalline lattice, after which the average misorientation of any given point is calculated relative to neighboring points. For the three sites, we observed values ranging from 0° to ~5° of misorientation, and this misoriented lattice tends to be concentrated along the shock fractures (Figure 12). We found that such misorientations are

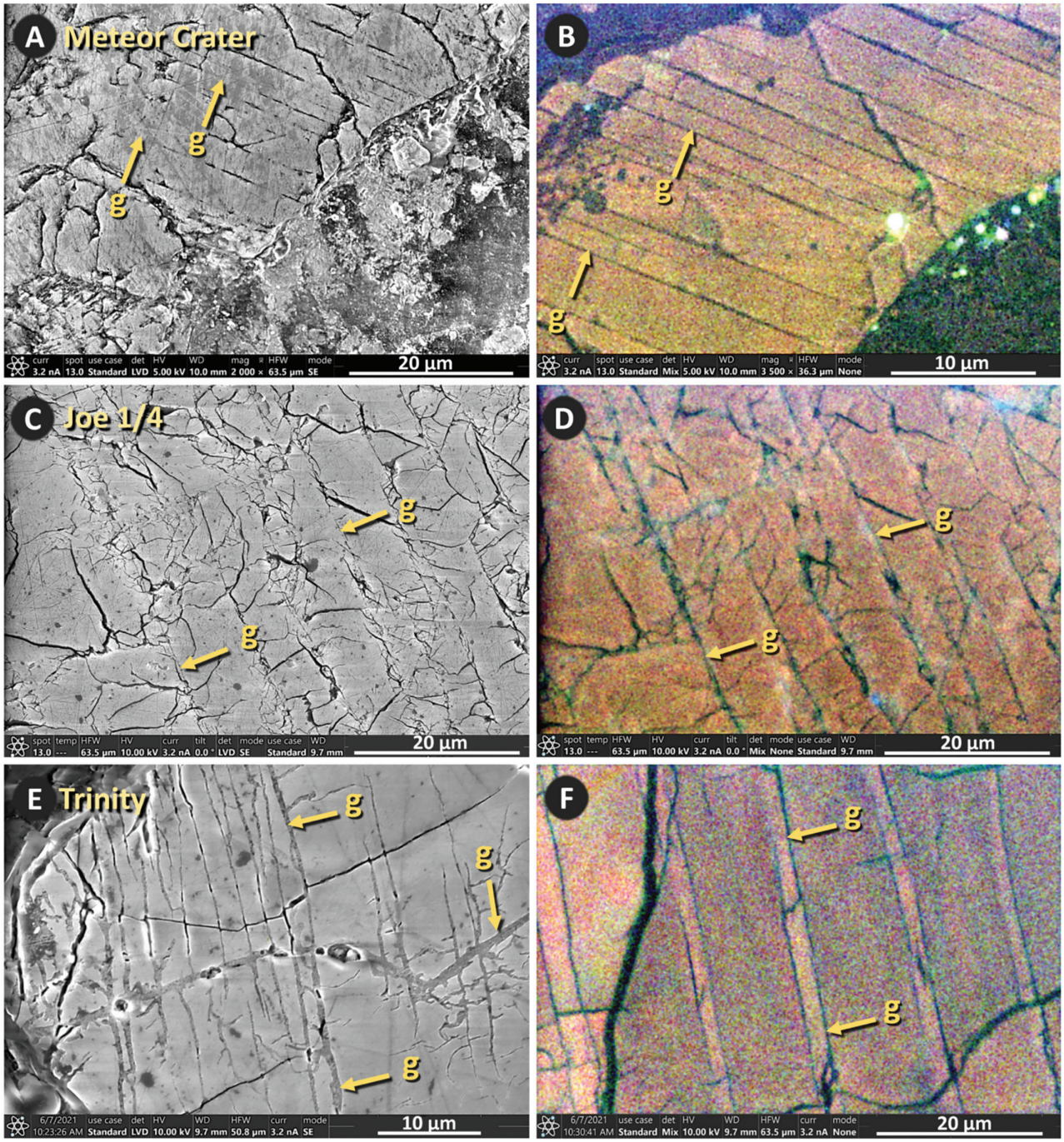

Figure 10: **SEM and cathodoluminescence (CL) images of shock fractures in quartz. (A, B)** Grain 14x-04a from Meteor Crater, Arizona. **(C, D)** Grain 09x14 from the Russian Joe-1/4 nuclear test. **(E, F)** Grain 32x08 from Trinity meltglass. The red arrows point to sub-parallel pairs of shock fractures in the SEM-BSE images (left-hand column) and CL images (right-hand column). In SEM-BSE images (left-hand column), yellow arrows point to thin, dark-gray bands of amorphous silica labeled "g." In the CL images (right-hand column), the bluish-gray-to-black bands at arrows labeled "g" indicate non-luminescent, glass-filled shock fractures. As confirmed by EDS, the material is amorphous silica (glass).

common in quartz with shock fractures, but are atypical in unshocked quartz grains (e.g., Figure 16).

Trinity grain 32x08 was scanned using SEM (Figure 13A) that recorded EBSD data with a beam width of ~20 nm and indexed the crystallographic patterns automatically (Figure 13B). This provides information about the orientation of the crystal at that spot relative to sample coordinates, generally defined by three Euler angles that relate sample

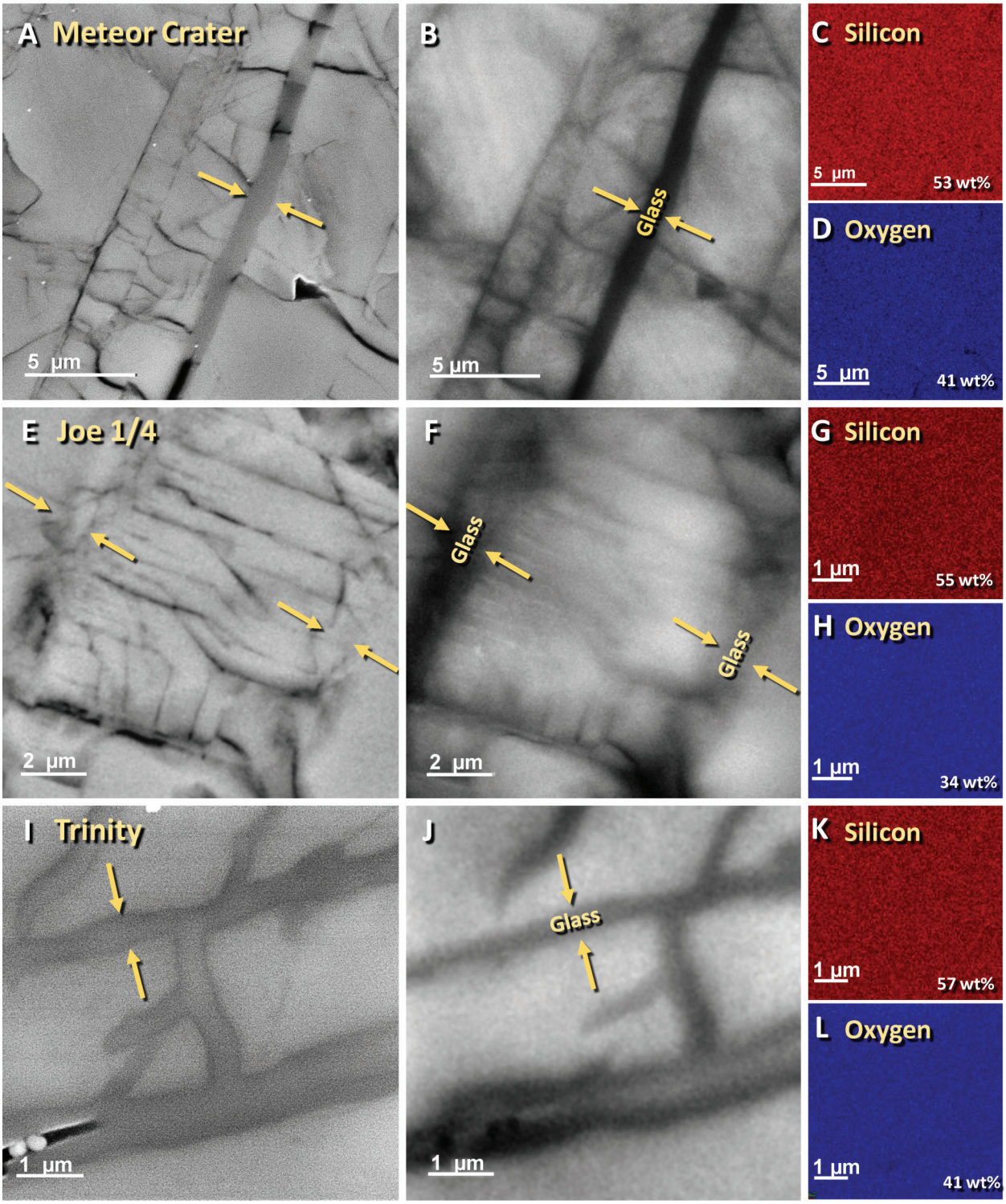

Figure 11: Images acquired using SEM, grayscale panchromatic cathodoluminescence (CL), and energy dispersive spectroscopy (EDS). (A-D) Grain #10x-12 from Meteor Crater, Arizona. **(E-H)** Grain #14x-04B from the Russian Joe-1/4 nuclear test. **(I-L)** Grain #32x08 from Trinity meltglass. In the SEM-BSE images (left-hand column), the yellow arrows point to shock fractures filled with gray material. In the gray-scale panchromatic CL images (spectrum: 185–850 nm; middle column), the yellow arrows point to the corresponding region, marked as glass. The gray-to-black color indicates that the filling material is non-luminescent, consistent with amorphous silica [21, 59, 63, 64]. The SEM-EDS panels (right-hand column) are of approximately the same field of view as in the left-hand column and confirm that the material is predominantly composed of silicon and oxygen (see EDS spectra for panels in Appendix, Figures S8–S12). Thus, the evidence indicates that the filling in the fractures is amorphous silica.

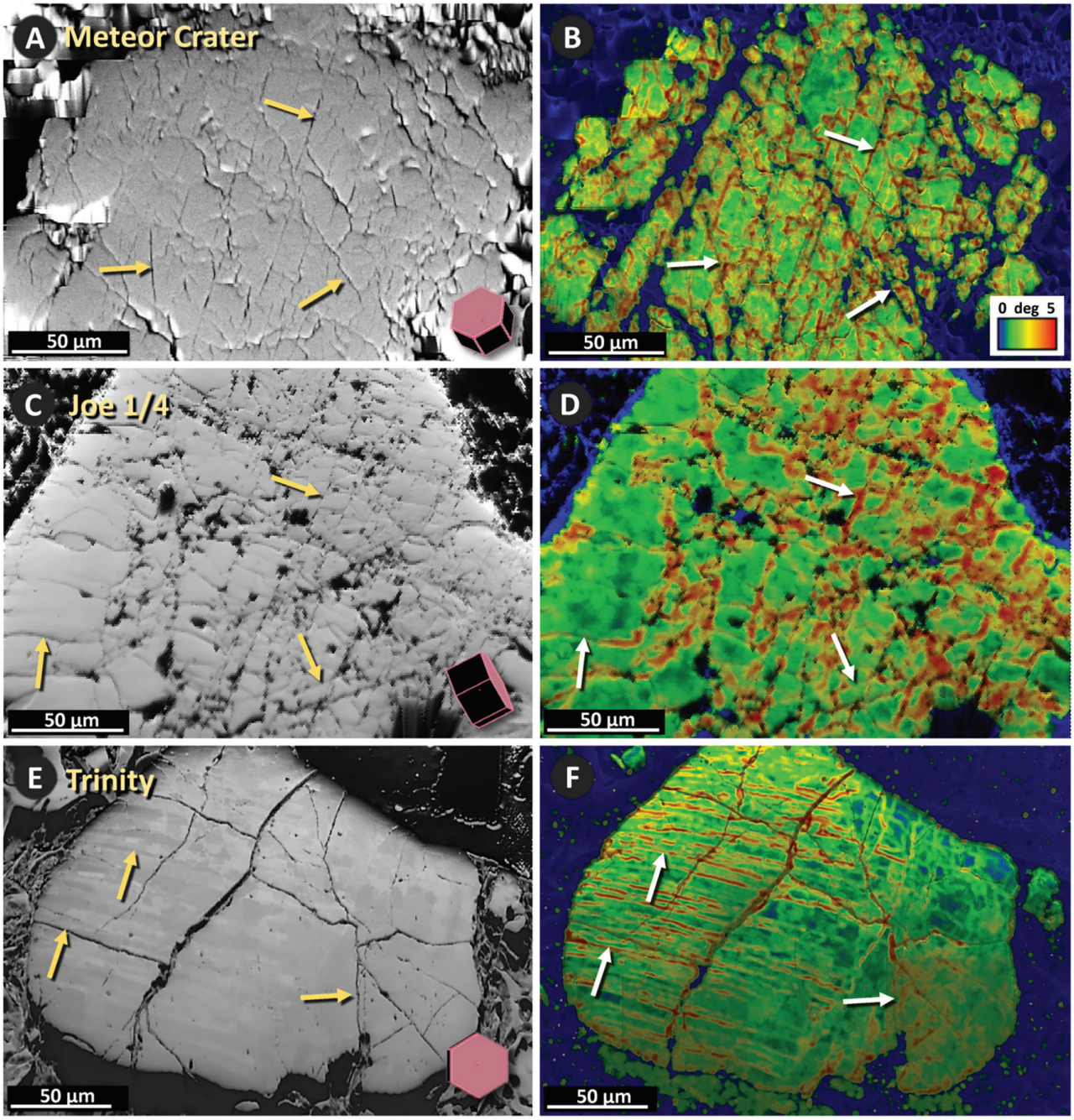

Figure 12: Images of fractures using EBSD. (A, B) Grain #10x-12 from Meteor Crater, Arizona. (C, D) Grain #14x-04B from the Russian Joe-1/4 nuclear test. (E, F) Grain #09x11 from Trinity meltglass. Images in the left-hand column show numerous oriented shock fractures, with arrows marking a few representative examples among the many fractures present. For a close-up view of the smaller fractures, see SEM-BSE image Figure 9E. For reference, the crystal representation at the lower right-hand of each image (left-hand column) represents the crystallographic orientation of that grain in which the *c*-axis is perpendicular to the red basal plane. A multi-colored misorientation scale is inset into the lower right-hand of panel **B** and applies to all images in the right-hand column. The colors represent the degrees of misorientation of the crystalline structure, ranging from 0 degrees (blue) to ~5 degrees (red). Note that the largest misorientation (i.e., damage) is concentrated along shock fractures. Some apparent disorientation might be an artifact of weaker quality diffraction patterns in the amorphous material or is due to surface irregularities near fractures, causing locally noisier orientation data.

and crystal coordinate systems. Figure 13C is a map over the same Trinity quartz grain with colors indicative of Euler angle f2; the Kikuchi pattern is shown in Figure 13D. The pole figure in Figure 13B shows that two main orientations are present across the selected area. The quartz grain has a *c*-axis roughly perpendicular to the sample surface (001

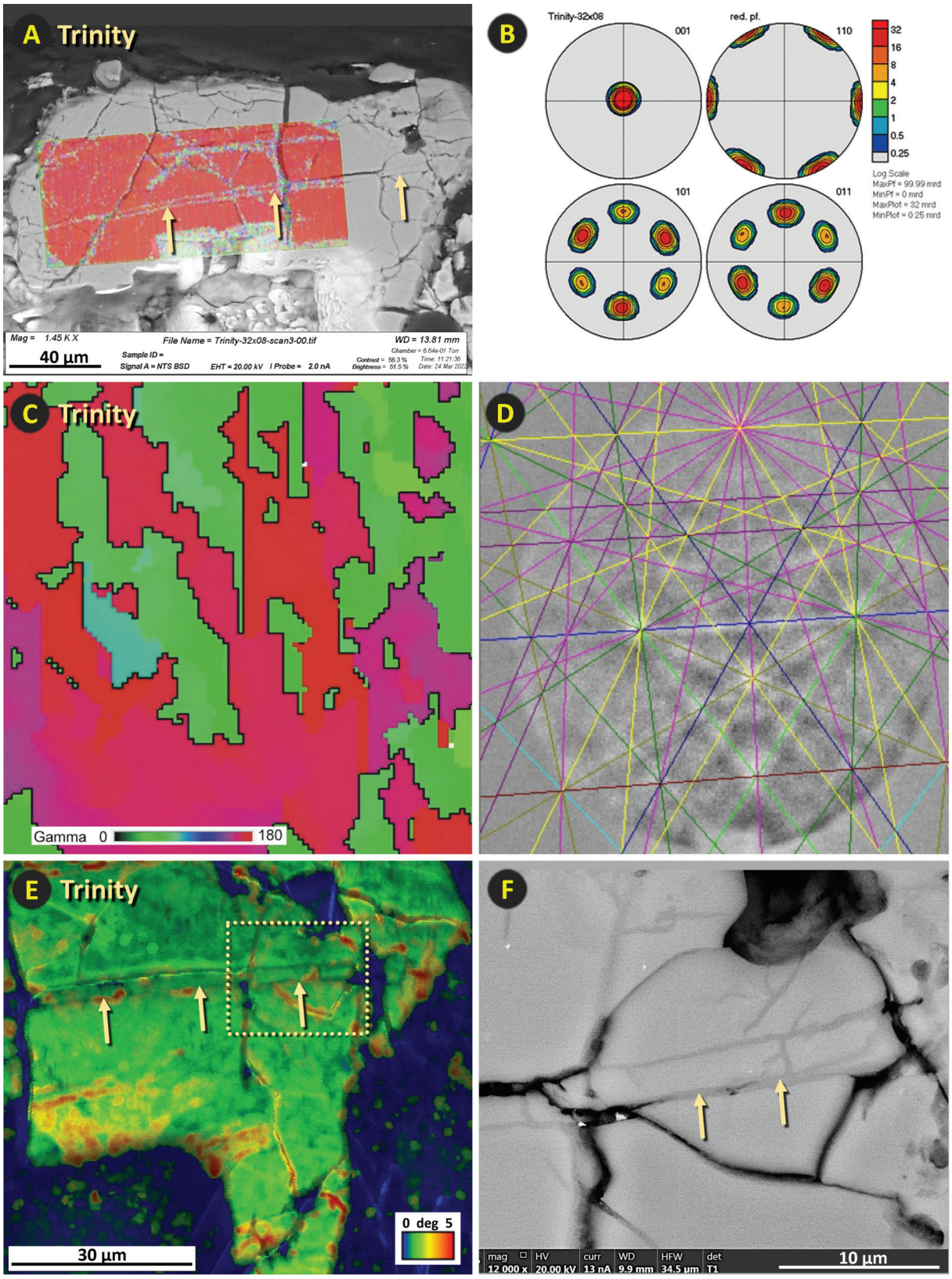

Figure 13: **Images of selected portions of shock-fractured quartz grain 32x08 from Trinity meltglass. (A)** EBSD "image quality" scan in red is superimposed on an SEM-BSE image; arrows mark a pair of oriented, sub-parallel shock fractures with damaged lattice, as indicated by the lack of the red EBSD signal. **(B)** Pole figures across the grain with the *c*-axis (0001) nearly perpendicular to the surface but with Dauphiné

twins that share two orientations rotated 60 degrees (101 and 011). **(C)** EBSD map of Euler angle gamma displays mainly two orientations (green and red). They are related by Dauphiné twinning (180 – 30 deg rotation around the *c*-axis, black outlines). Equal area projection. **(D)** Kikuchi patterns corresponding to EBSD scan in panel **C**. **(E)** Image quality and local orientation spread (LOS) image of lattice misorientations (yellow to red) that correspond to the sub-parallel shock fractures at arrows. **(F)** Close-up SEM-BSE image of oriented shock fractures, marked by gold-dotted box in panel **E**. Medium gray areas represent amorphous silica, as separately confirmed by SAD, FFT, and TEM-EDS.

pole figure) and two orientations of rhombohedral planes (101 and 011) related by a 60° (180°) rotation around the *c*-axis. This orientation relationship is known as Dauphiné twinning, which can form in multiple ways: during growth, during the phase transition from hexagonal high quartz to trigonal low quartz, during mechanical deformation, or during recrystallization after thermal shock. Several studies have observed Dauphiné twins in quartz subjected to stress (e.g., Schubnikow and Zinserling [67]; Tullis [68]; and Wenk et al. [41]). From the Euler angle relationships, twin boundaries can be defined, and the Dauphiné twin boundaries are plotted with black outlines in Figure 13C.

EBSD "grain reference orientation deviation" values superimposed on EBSD "image quality" values

Orientation deviation maps (Figure 14) assist with visualizing the distribution of local lattice angular misorientations by color-coding the variations. EDAX's EBSD software analyzes and colorizes individual points to illustrate any rotation of the crystalline lattice around an arbitrary common point on the grain with a wide range of colors that each represents areas with short-range misorientations relative to the common point.

Several of the grains in Figure 14 exhibit shock fractures that are curved. As the shock fractures formed, the lattice may have become distorted at high ambient temperatures or by shock melting, as suggested by Buchanan and Reimold [16] and Reimold and Koeberl [13].

EBSD "inverse pole figure" values superimposed on EBSD "image quality" values

The inverse pole figures (**right-hand column** of Figure 14) reveal variations in the lattice axes of quartz relative to a frame of reference, which, in these examples, is the (0001) basal plane. The EBSD results indicate that these are monocrystalline grains. In each case, measurements show that areas of quartz grains known as Dauphiné twins are rotated 60° relative to the *c*-axis. Dauphiné twinning is undetectable by standard optical microscopy and SEM but can easily be seen using EBSD.

For the shocked quartz analyzed in our study, Dauphiné twins typically align with the trend of the shock fractures, suggesting that they crystallized as the fractures formed under high stress or formed after the grain fractured as it cooled from the high shock temperatures. It has long been recognized that Dauphiné twins form when quartz is subjected to mechanical stress [67]. Later, Wenk et al. [41] further concluded that Dauphiné twinning occurs under high thermal and mechanical stress. Subsequently, Wenk et al. [42] reported that Dauphiné twinning provides evidence for an impact-related origin of shocked quartzite collected from the Vredefort crater in South Africa.

Natural and tectonically deformed quartz grains

This study used optical microscopy and SEM-EDS to investigate hundreds of HF-etched natural, unshocked quartz grains and tectonically deformed grains. These grains commonly displayed fractures, but SEM-EDS observed none to contain silica. In addition, although Dauphiné twins are nearly ubiquitous in all quartz grains, including unshocked or tectonically deformed grains, they are typically distributed randomly (Figures 15 and 16). This random distribution is unlike shock-fractured quartz grains in which Dauphiné twins are nearly always oriented with the fractures.

Additional imagery showing variations in shock-fractured quartz

Given the importance of imagery for this investigation, we provide additional examples from Trinity, Joe, and Meteor Crater (Figures 17–19). These illustrate the wide variation in shock fracture characteristics that we documented. These images were acquired using the same analytical techniques presented above.

Potential formation mechanisms of shock fractures

This investigation supports the hypothesis that glass-filled shock fracturing can occur in nuclear detonations and crater-forming impact events. Although the characteristics of these two events are mostly dissimilar, there are essential similarities in the shock effects. Both events produce enormous temperatures and pressures capable of melting quartz and producing shock metamorphism. The most important similarity is that, in both events, the fireball's shockwave is coupled with Earth's surface. This situation is unlike high-altitude nuclear detonations in which the fireball does not intersect the Earth's surface. This coupling appears essential for providing the following mechanisms to produce amorphous silica in shocked fractures.

Shock fracturing by compression

Evidence indicates that shock fractures, as well as shock PDFs and PFs, form when quartz grains are subjected to shock pressures above their Hugoniot elastic limit (HEL), which, for quartz, ranges from ~3–15 GPa [27]. This pressure

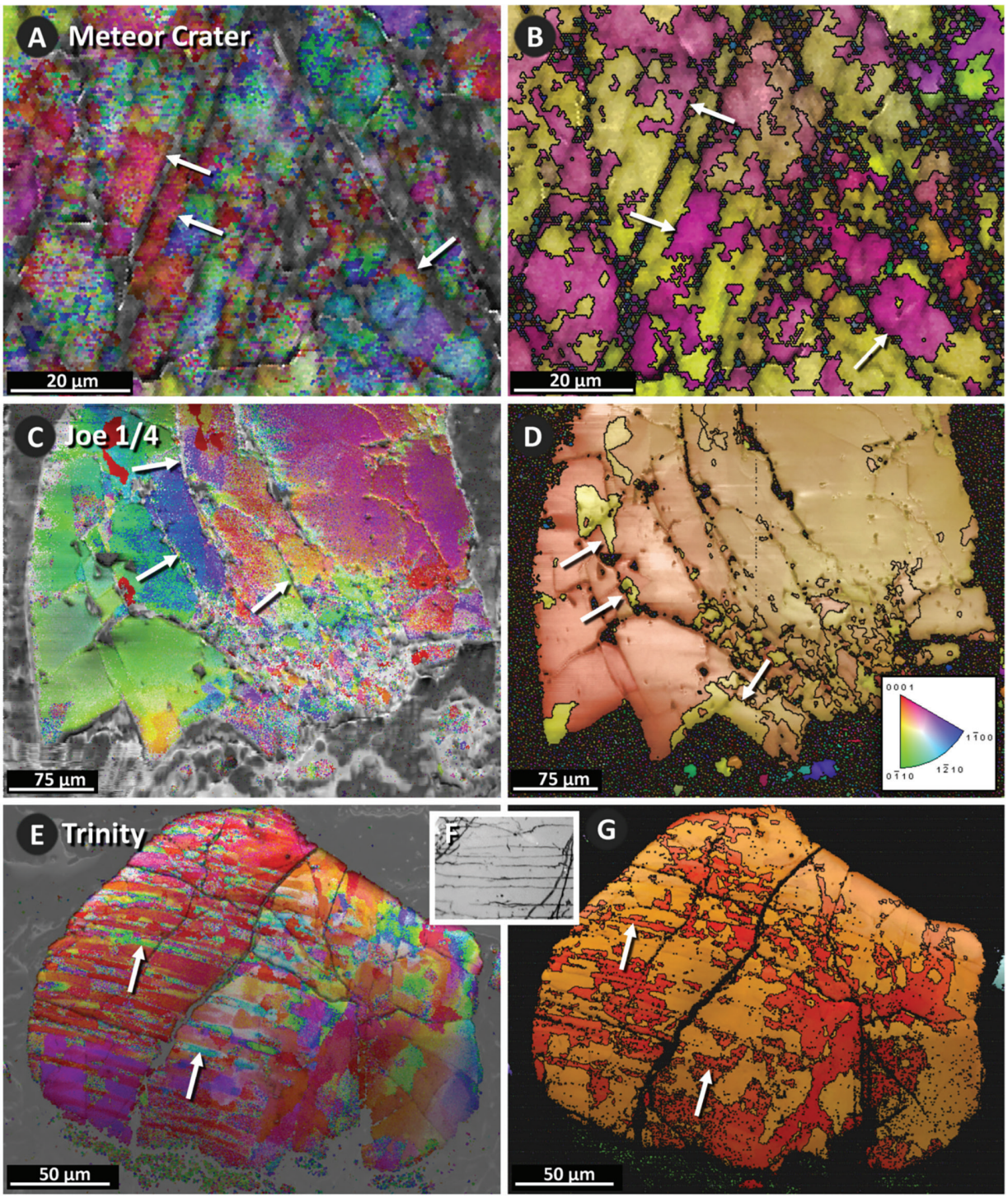

Figure 14: EBSD images using "orientation deviation" superimposed on "image quality" and EBSD "inverse pole figure" superimposed on "image quality." **(A, B)** Grain #10x-12 from Meteor Crater, Arizona. **(C, D)** Grain #19x-12C from the Russian Joe-1/4 nuclear test. **(E-G)** Grain #09x11 from Trinity meltglass. **(A, C, E** in the **left-hand column)** Orientation deviation analyses show the crystalline misorientation of the grain relative to an average value. Note that the misorientations tend to align with shock fractures (gray-to-black colored) at the white arrows. **(F)** Epi-illumination image showing open fractures corresponding to arrow in panel **C**. **(B, D, G** in right-hand column**)** Inverse pole figure analyses illustrate the axes of rotation of areas around the *c*-axis. In each figure, the white arrows mark black-outlined Dauphiné twins that are rotated 60° around the *c*-axis of these monocrystalline quartz grains. This twinning is represented by the magenta color in panel **B**, yellow color in **D**, and red in **G**. Note that most Dauphiné twins are oriented along shock fractures (gray-to-black colored), suggesting that the twinning formed synchronously with the shock fractures and is common in all quartz grains from the three sites investigated here. The inset legend in panel **D** shows the color-coded Miller-Bravais crystalline axes for all six panels.

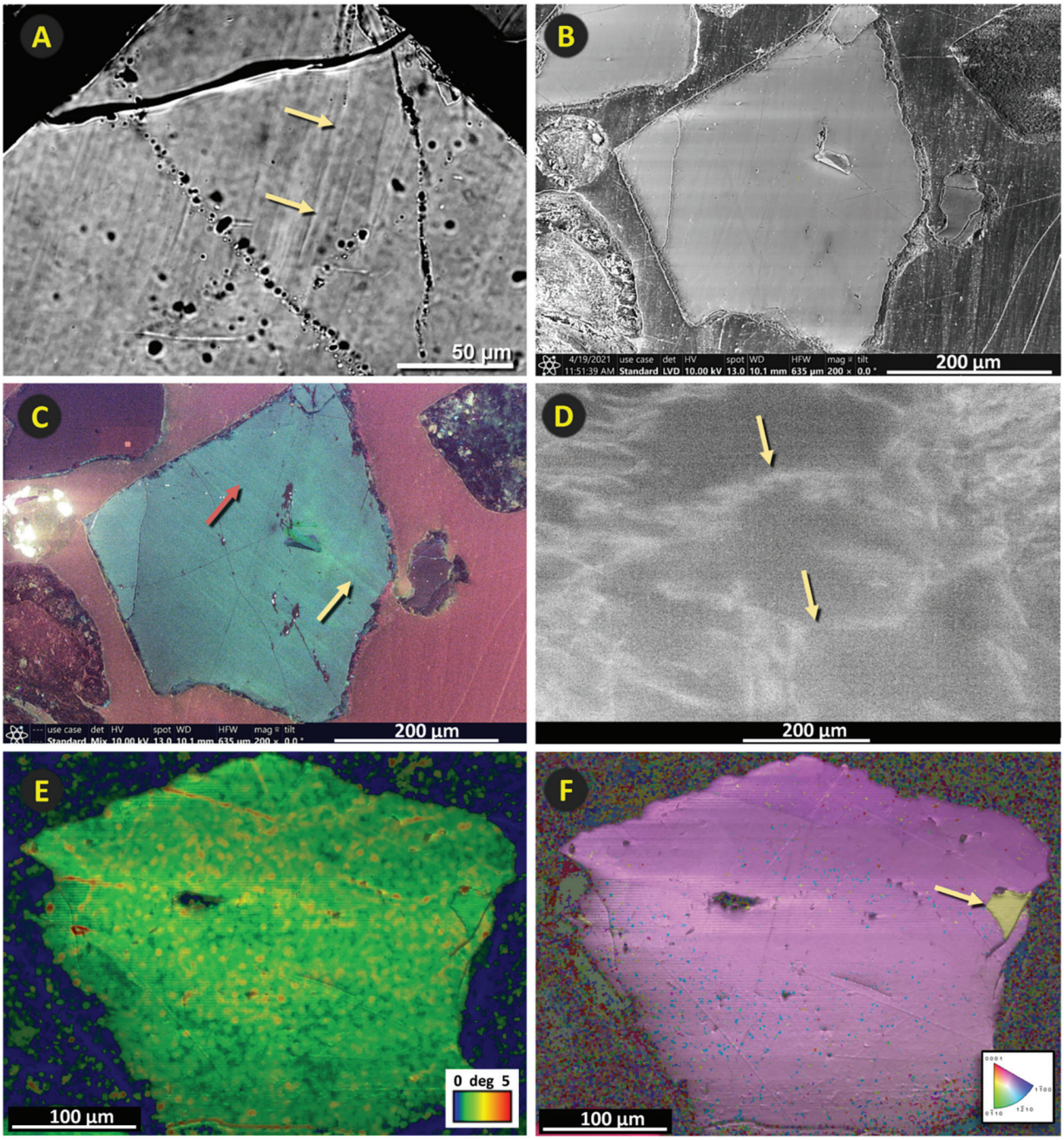

Figure 15: Tectonically-deformed quartz from a non-impact site in Syria. (A) Optical microscopy image shows tectonically-deformed lamellae, marked by yellow arrows. **(B)** SEM-BSE image: tectonic lamellae are not visible on the surface. **(C)** Cathodoluminescence (CL). The tectonic lamellae are faintly visible as blue streaks in the grain. Blue luminescence indicates that the quartz is natural and unshocked [21, 59, 63, 64]. The red arrow marks the extraction location of the ion beam (FIB) foil for use with TEM. **(D)** Bright-field TEM image with no parallel lamellae; yellow arrows mark irregular areas characteristic of dislocations in the quartz. **(E)** EBSD image quality (IQ) and local orientation spread (LOS) image shows no significantly aligned misorientations. **(F)** EBSD IQ superimposed on inverse pole figure (IPF); the single Dauphiné twin (yellow arrow) is not oriented with any features in the grain, except the single fracture to the right. In this grain, the tectonic lamellae are only visible in the optical and CL images and not in other analyses, as they are in shock fractures. These multiple techniques enable differentiation between non-shock tectonic lamellae and impact-related shock fractures.

range corresponds with that estimated for the nuclear tests of Trinity and Joe-1/4. A pressure database [69] reveals that in quartz, velocities of the pressure wave range from 6.3 to 6.9 km/sec, depending on a quartz grain's orientation.

High shock pressures commonly produce quartz phases called coesite or stishovite. However, we found no evidence of these phases previously observed at Meteor Crater [2, 3, 32, 48, 49, 70–73]. The absence of these

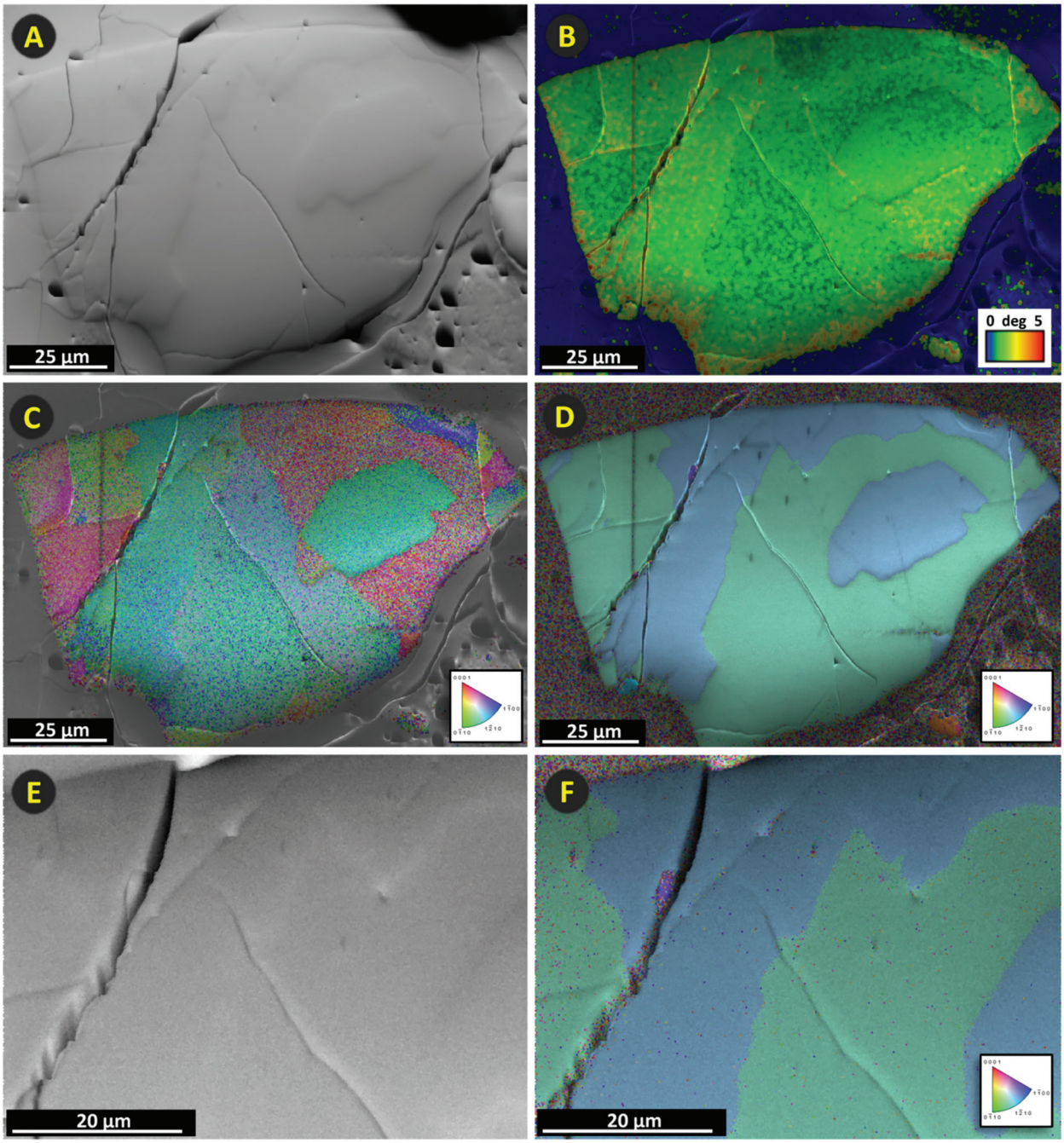

Figure 16: **Natural, fractured, and unshocked quartz from the Russian Joe-1/4 site. (A)** The EBSD image shows a few fractures, but they are not glass-filled. **(B)** EBSD image quality superimposed on local orientation spread shows no shock fractures aligned with locally misoriented lattice. **(C)** EBSD image quality (IQ) and grain reference orientation deviation (GROD) show no pattern of misoriented lattice compared to the grain's average orientation. **(D)** EBSD image quality (IQ) and inverse pole figures (IPF) illustrate variations in the lattice axes of quartz relative to a chosen crystal reference frame, which for these grains is the (0001) basal plane. These color variations represent Dauphiné twinning (blue and green) but are not oriented along the fractures. **(E)** Close-up SEM-BSE image of quartz grain. **(F)** SEM-BSE and EBSD inverse pole figures. This grain is fractured, but the fractures are not oriented as in shock fractures. In addition, no amorphous silica was found associated with the lamellae. No well-oriented lamellae are visible in any of these images.

phases supports the hypothesis that the shocked grains investigated in this study from Trinity, Joe, and Meteor Crater formed at the lower range of shock pressures, estimated to be ≤8 GPa.

Shock fracturing by tension

In both airbursts and crater-forming events, the fracturing of quartz grains may also occur from tensile forces and spallation [26, 35, 37, 74–76]. This shock occurs when a

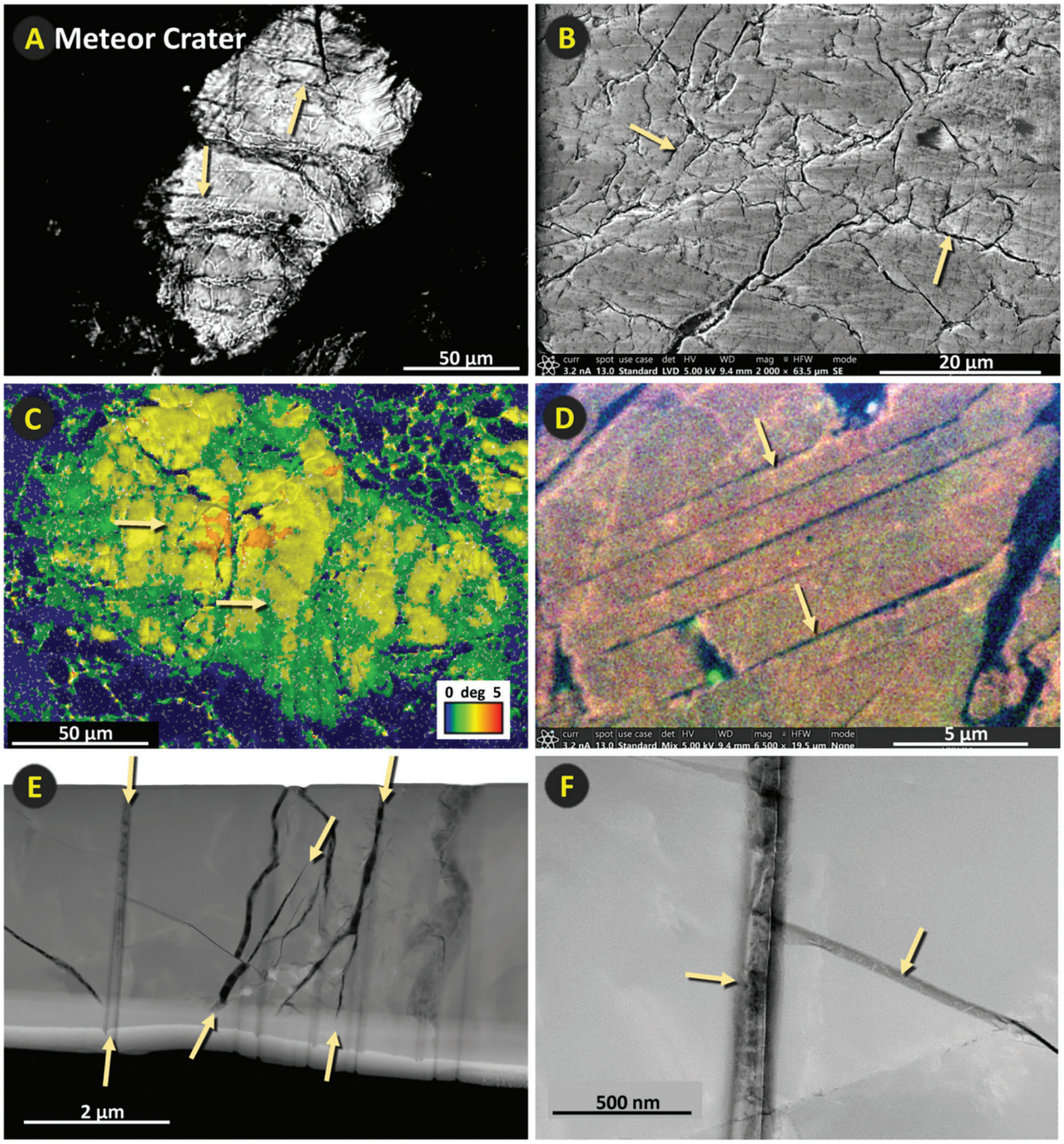

Figure 17: **Images of selected portions of shock-fractured quartz grain 09x-11 from Meteor Crater. (A)** Optical photomicrograph. Arrows mark selected shock fractures. **(B)** SEM-BSE image. **(C)** EBSD image quality (IQ) and grain average image quality (GAIQ). Green areas at the arrows represent areas that correspond with shock fractures. **(D)** Cathodoluminescence (CL) image of non-luminescent gray-to-black areas at arrows indicating amorphous silica in areas corresponding to oriented shock fractures. **(E)** Bright-field TEM image of open, glass-filled shock fractures. **(F)** Close-up TEM image of glass-filled shock fractures.

compressive shockwave enters a material, such as a quartz grain, and then reflects off the opposite grain boundary, producing a rarefaction wave that fractures the grain in the opposite direction. The shockwave may occur at < 1 GPa and does not need to exceed quartz's Hugoniot elastic limit (HEL) to cause tensile damage. This process frequently produces the most mechanical damage because the tensile strength of quartz is typically lower than its compressive strength. In this study, tensile fracturing is considered to be the most common formation process.

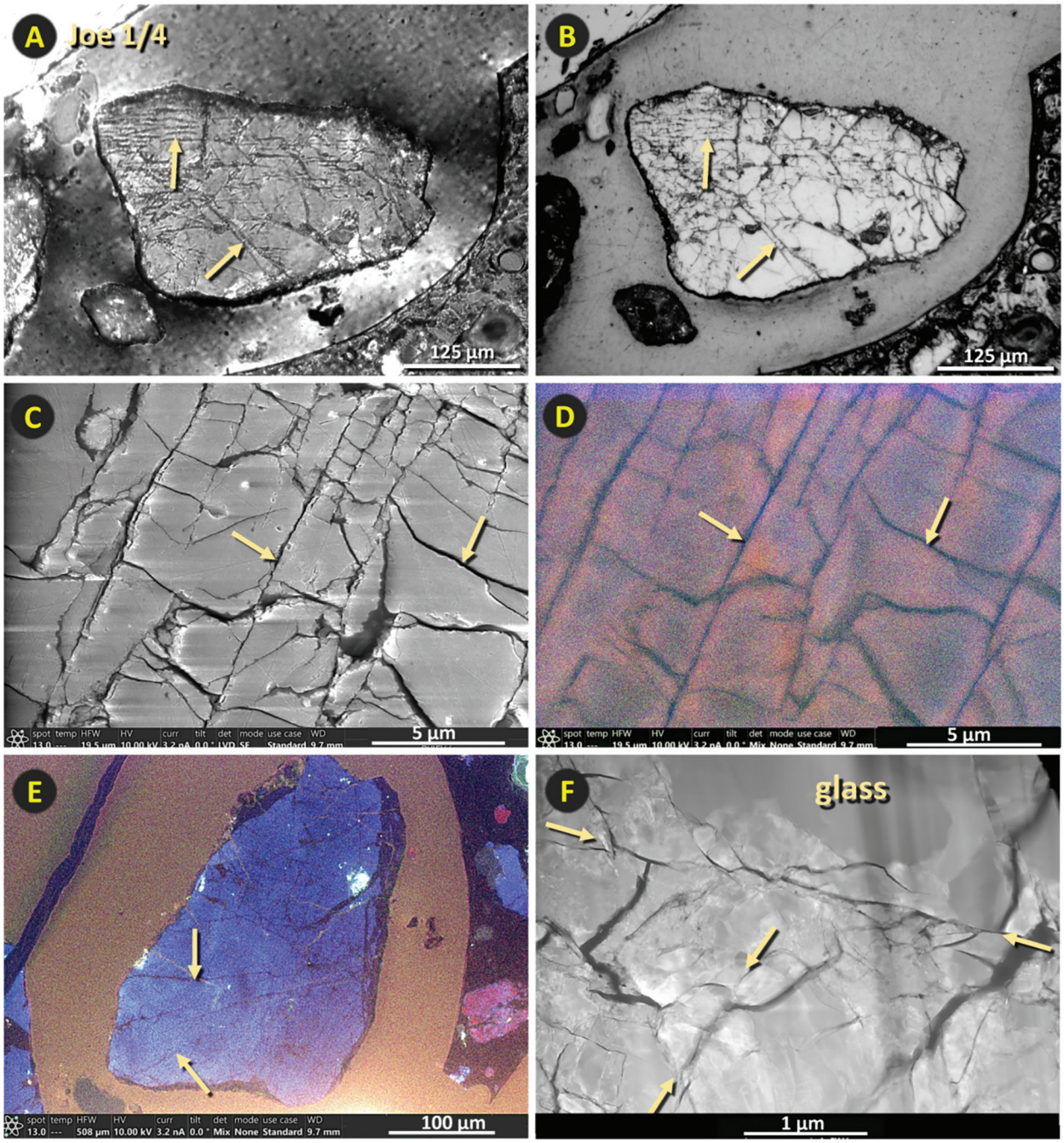

Figure 18: Images of selected portions of shock-fractured quartz grain 12x12 from the Joe-1/4 atomic test site. **(A)** Optical photomicrograph with arrows pointing to selected shock fractures. Yellow arrows mark fractures. **(B)** EPI photomicrograph of the same view as panel **A**. **(C)** SEM-BSE image. **(D)** Cathodoluminescence (CL) image shows non-luminescent black lines at arrows indicative of amorphous silica, as confirmed by TEM in panel **F**. Approximately the same view as in panel **C**. **(E)** Cathodoluminescence (CL) image shows blue-colored, unshocked quartz matrix containing non-luminescent black lines at arrows indicative of amorphous silica along shock fractures. **(F)** TEM image of oriented and unoriented shock fractures. The notation "glass" marks a darker gray subrounded area composed of amorphous silica.

Thermal shock-metamorphism

For shock fractures to form in quartz, the crystalline lattice must experience high stress and strain, not just from high pressures but also typically from high-temperature gradients. Nuclear tests like Trinity generate fireballs with extreme temperatures that may rise to ~200,000 °C within 10^{-4} sec but then, after 3 sec, drop to below the melting point of quartz [77]. Such extreme, short-lived temperatures followed by rapid quenching can fracture quartz grains due to sudden thermal expansion followed by rapid cooling. In

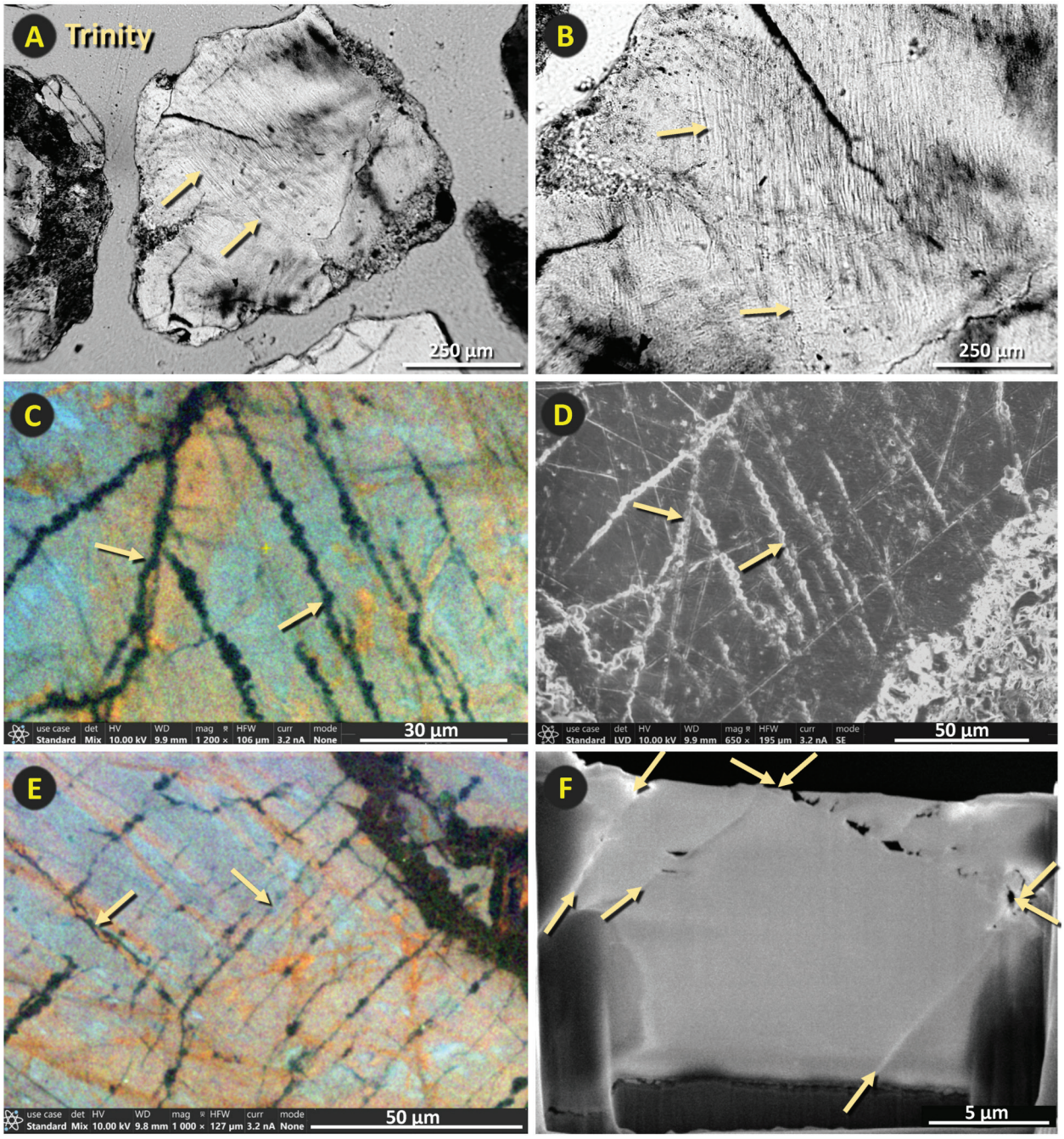

Figure 19: Images of selected portions of shock-fractured quartz grain 30x08 from Trinity JIE grains sample. **(A)** Optical photomicrograph of selected shock fractures at arrows. **(B)** Close-up optical photomicrograph. **(C)** Cathodoluminescence (CL) image of non-luminescent, black lines at arrows indicative of amorphous silica associated with shock fractures, as confirmed by TEM. **(D)** SEM-BSE image of approximately the same grain region as shown in panel **C**. **(E)** Another CL image of non-luminescent, black lines indicates the presence of amorphous silica. **(F)** TEM image with arrows marking three directions of shock fractures.

addition, the intense thermal and gamma radiation may heat the quartz grains to near-melting and, thus, reduce the pressures needed to form shock fractures. These thermal processes appear responsible for forming Dauphiné twinning in alignment with the shock fractures. To our knowledge, this is the first report of such a connection.

Most importantly, we concur with the jetting hypothesis by Kieffer [32] that high temperatures appear to vaporize quartz grains and sediment, after which high pressures inject molten silica or vapor into the fractures and any other zones of weakness in exposed quartz grains [33, 37]. We infer that molten silica might enter quartz grains along multiple

possible zones of weakness: (i) fractures produced by the shockwave; (ii) fractures produced by high temperatures; (iii) pre-existing quartz fractures; (iv) new fractures that form along pre-existing PDFs and PFs; (v) new fractures along pre-existing tectonic lamellae; and (vi) new fractures along pre-existing subgrain boundaries. In the cases of the pre-existing features, the shock fracturing process overprints and modifies the existing features. Even though these types of fractures may form under substantially different shock and non-shock conditions, all have one common characteristic: they became filled with amorphous silica, as described next.

Previous studies of amorphous silica in quartz grains

There have been many studies that identified amorphous silica in quartz. Kieffer [32] analyzed shocked sandstone from Meteor Crater and concluded that impact-related glass-filled fractures began to form at 5.5 GPa but not at lower pressures (Table 2). Christie and Ardell [18] performed shock compression experiments on large quartz cylindrical crystals and noted amorphous silica that filled the fractures at a confining pressure of 1.5 GPa. Kenkmann et al. [78] performed shock experiments on 1.5-mm-wide cylindrical samples of quartz, and using moderate shock pressures of 6–34 GPa, they could generate veins of amorphous silica that were 1–6 μm wide. Kowitz et al. [11, 15, 46] conducted detailed laboratory experiments to determine the lower pressure limit for forming shock features called "sub-planar, intra-granular fractures." [11] In their experiments, a steel plate was explosively driven into cylinders of quartz-rich sandstone at pressures of 5, 7.5, 10, and 12.5 GPa. Visible shock fractures and amorphous silica (~1.6 wt%) first appeared at 5 GPa [11], similar to the results of Kieffer [32]. Carl et al. [7] conducted experiments demonstrating that extensive amorphization of quartz begins at ~10 GPa. In quartz grains experimentally shocked at 5 to 17.5 GPa, Fazio et al. [5] observed glass veins composed of amorphous silica generally thicker than 50 nm, extending several microns in length. Wilk et al. [6] found amorphous silica in experimentally shocked rocks called shatter cones that formed at low shock pressures of 0.5–5 GPa. Laboratory shock experiments by Martinelli et al. [79] used quartz crystals with a minimum diameter of 3400 μm, larger than we tested. The reported compression applied was as low as 0.2 GPa; the maximum compression applied is unclear but appears to have been <1 GPa.

In summary, these studies report the formation of amorphous silica in fractures produced by minimum shock pressures averaging 4.2 GPa (range 0.2 to 10 GPa), with 5 of the 8 studies reporting ~5 GPa as the minimum observed pressure. No experimental study has ever reported glass-filled fractures in natural quartz grains, nor have they been reported in natural quartz grains exposed to non-impact processes, such as volcanism and tectonism [19, 80]. The existing evidence supports their formation during nuclear detonations and hypervelocity impact events. In addition, Ernstson et al. [26, 34, 36, 37, 76, 81, 82], Moore et al. [83], Demitroff et al. [84], and Mahaney et al. [85] have reported shock-metamorphosed quartz in multiple proposed airbursts during the Cenozoic.

Proposed model for producing shock fractures

To summarize, we propose that shock fractures form in the following sequence. (i) Fractures in quartz grains either preexist or are produced by the high-pressure shockwave and thermal pulse both by compression and tensioning; (ii) the blast vaporizes some quartz grains, and this vapor is transported away from ground zero in the expanding fireball; (iii) the outer surfaces of some quartz grains melt at >1720 °C, the melting point of quartz; (iv) the extreme pressures inject molten silica or silica vapor into the fractures; and (v) both thermal and pressure shock may cause further random melting on the exteriors and in the interiors of some grains.

Future studies

Several studies [34, 36, 37, 75, 86] have reported evidence that shock fractures are produced in cosmic airbursts when a high-pressure, high-temperature fireball intersects the surface, similar to the nuclear airbursts described here. These cosmic airbursts may produce shallow craters rather than classic hard-impact craters. We suggest that future studies investigate the hypothesis that low-shock, glass-filled shock fractures are produced in quartz grains during near-surface cosmic airbursts. Similarly, we suggest further research to improve our understanding of glass-filled fractures in hard-impact craters of all sizes.

Conclusions

Glass-filled shock lamellae and fractures are considered to be definitive indicators of a crater-forming impact event and are widely accepted to form at extreme pressures of ~5 to >30 GPa. However, most previous studies of shocked quartz were conducted on large craters and on easily recognizable quartz grains that had been shocked at the higher end of that pressure range. Consequently, there is limited knowledge about the characteristics of quartz grains minimally shocked at lower shock pressures.

This study confirmed previously reported low-shock fractures in quartz at Meteor Crater, a relatively small 1.2-km-wide impact event. Most importantly, we confirmed that similar low-shock fractures also form in near-surface nuclear airbursts, where the fireball and the blast wave reach the surface and no hard-impact crater forms. Despite being static instead of moving at high velocity, these nuclear airbursts create ambient conditions of high pressures and temperatures that are proposed to be similar to those near-surface

cosmic airbursts in which the shockwave couples to Earth's surface.

We observed that these low-grade shock fractures: (i) are either void or filled with glass; (ii) range from near-planar to curvilinear; (iii) are commonly sub-parallel in orientation; (iv) are commonly spaced microns apart; (v) are typically less than one micron thick; (vii) are typically closely aligned with Dauphiné twins; and (viii) appear to form at <5 GPa. Notably, Dauphiné twinning occurs during exposure to high pressures or high temperatures, after which portions of the grains recrystallize in alignment with the fracture patterns. Multiple studies have concluded that when amorphous silica is present within fractures, it allows for the unequivocal differentiation between impact-related shock fractures and the glass-free lamellae that mark slow-strain tectonic deformation. The same principle applies to shock fractures formed in nuclear detonations. Thus, we conclude that these shock fractures cannot be of tectonic origin.

The discovery of shock fractures in quartz exposed to nuclear airbursts has important implications. It suggests that shock metamorphism may also occur during a near-surface airburst of an asteroid or comet if the bolide disintegrates close enough to the Earth's surface to generate large shock pressures. The protocol reported here may help identify low-shock fractures in quartz from previously unknown, near-surface cosmic airbursts and small crater-forming impact events in the past.

Data availability

All essential data are published here. No more sample material is available from the authors for Trinity, Joe-1/4, or Meteor Crater.

Acknowledgments

We are grateful to five anonymous reviewers whose thoughtful comments helped us to improve the manuscript. We also gratefully acknowledge the long-standing contributions of co-author Ted Bunch, a highly valued colleague and contributor, who passed away while writing this manuscript. We thank Yiming Zhang, University of California, Berkeley, for contributing to EBSD analyses. We also gratefully acknowledge Jim Eckles and Byron Ristvet for providing crucial samples from the Trinity and the Joe-1/4 site, respectively (for details, see Appendix, Methods). We greatly appreciate constructive comments from Maartje Hamers, Universiteit Utrecht; Susan Kieffer, the University of Illinois at Urbana-Champaign; and Peter Schultz, Brown University. We also appreciate access to the CAMCOR facilities at the University of Oregon and the Electron Microscopy and Surface Analysis Laboratory at the University of Utah with assistance from EDAX, LLC. This work made use of the University of Utah's USTAR shared facilities supported, in part, by the MRSEC Program of the NSF under Award #DMR-1121252. H.-R.W. appreciates the support from NSF (Grants EAR 1343908 and EAR1464014) and DOE (Grant DE-FG02-05ER15637). G.K. appreciates the support from the Czech Science Foundation (Grant 23-06075S). We also thank the thousands of donors and members of the Comet Research Group who have been crucial in making this research possible. In particular, we thank Eugene Jhong, who provided substantial gifts to the University of South Carolina (C.R.M.) and the University of California, Santa Barbara (J.P.K.) in support of this research. We also thank George Howard and the Cosmic Summit for their contributions to promote this research.

Author contributions

Conceptualization: R.E.H., H.-R.W., J.P.K., T.E.B., G.K., A.W. Formal analysis: R.E.H., H.-R.W., J.P.K., T.E.B., C.R.M., M.A.L., G.K., A.V.A., K.L., J.J.R., M.W.G., S.M., J.P.P., R.P., M.N., A.W. Investigation: R.E.H., H.-R.W., J.P.K., T.E.B., C.R.M., M.A.L., G.K., A.V.A., K.L., J.J.R., M.W.G., S.M., J.P.P., R.P., M.N., A.W. Writing-original draft: R.E.H., H.-R.W., J.P.K., T.E.B., C.R.M., M.A.L., G.K., A.W. Writing-review and editing: R.E.H., H.-R.W., J.P.K., C.R.M., M.A.L., G.K., A.W. Funding acquisition: R.E.H., H.-R.W., J.P.K., G.K., A.W. All authors reviewed and approved this manuscript.

Competing interests

The Comet Research Group (CRG), a 501(c) (3) nonprofit charitable organization, provided research funding. J.P.K., M.A.L., C.R.M., and A.W. volunteer their time as cofounders and directors of CRG. No co-author receives a salary, compensation, stock, or any other financial benefit from CRG, except for co-authors A.W. and M.A.L., who benefit from tax deductions for donations to CRG. A.W. is a co-author of a book unrelated to the focus of this study; he donates all proceeds to CRG.

References

[1] Grieve, R.A.; Kring, D.A. The Geologic Record of Destructive Impact Events on Earth. *Comet/Asteroid Impacts and Human Society: An Interdisciplinary Approach*; 2007; pp. 3–24.

[2] Eby, G.N.; Charnley, N.; Pirrie, D.; Hermes, R.; Smoliga, J.; Rollinson, G. Trinitite Redux: Mineralogy and Petrology. *Am. Mineral.* **2015**, *100*, 427–441, doi:10.2138/am-2015-4921.

[3] Lussier, A.J.; Rouvimov, S.; Burns, P.C.; Simonetti, A. Nuclear-Blast Induced Nanotextures in Quartz and Zircon within Trinitite. *Am. Mineral.* **2017**, *102*, 445–460, doi:10.2138/am-2017-5739.

[4] Wannier, M.M.; de Urreiztieta, M.; Wenk, H.-R.; Stan, C.V.; Tamura, N.; Yue, B. Fallout Melt Debris and Aerodynamically-Shaped Glasses in Beach Sands of Hiroshima Bay, Japan. *Anthropocene* **2019**, *25*, 100196, doi:10.1016/j.ancene.2019.100196

[5] Fazio, A.; Pollok, K.; Langenhorst, F. Experimental Evidence for Mechanical Brazil Twins as an Indicator of Low-Pressure Shock Metamorphism (<17.5 GPa). *Geology* **2018**, *46*, 787–790, doi:10.1130/G40198.1.

[6] Wilk, J.; Hamann, C.; Fazio, A.; Luther, R.; Hecht, L.; Langenhorst, F.; Kenkmann, T. Petrographic Investigation of Shatter Cone Melt Films Recovered from MEMIN Impact Experiments in Sandstone and iSALE Modeling of their Formation Boundary Conditions. *Meteorit. Planet. Sci. U S A.* **2018**, *53*, 1569–1593, doi:10.1111/maps.13179.

[7] Carl, E.R.; Mansfeld, U.; Liermann, H.P.; Danilewsky, A.; Langenhorst, F.; Ehm, L.; Trullenque, G.; Kenkmann, T. High-Pressure Phase Transitions of α-Quartz Under Nonhydrostatic Dynamic Conditions: A Reconnaissance Study at PETRA III. *Meteorit. Planet. Sci. U S A.* **2017**, *52*, 1465–1474, doi:10.1111/maps.12840.

[8] French, B.M.; Koeberl, C. The Convincing Identification of Terrestrial Meteorite Impact Structures: What Works, What Doesn't, and Why. *Earth Sci. Rev.* **2010**, *98*, 123–170, doi:10.1016/j.earscirev.2009.10.00.

[9] Bohor, B.; Fisler, D.; Gratz, A.J. Distinguishing between shock and tectonic lamellae with the SEM. In Proceedings of the Lunar and Planetary Science Conference, 1995; p. 145.

[10] Koeberl, C.; Reimold, W.U.; Cooper, G.; Cowan, D.; Vincent, P.M. Aorounga and Gweni Fada Impact Structures, Chad: Remote Sensing, Petrography, and Geochemistry of Target Rocks. *Meteorit. Planet. Sci.* **2005**, *40*, 1455–1471, doi:10.1111/j.1945-5100.2005.tb00412.x.

[11] Kowitz, A.; Schmitt, R.T.; Uwe Reimold, W.; Hornemann, U. The First MEMIN Shock Recovery Experiments at Low Shock Pressure (5–12.5 GPa) with Dry, Porous sandstone. *Meteorit. Planet. Sci.* **2013**, *48*, 99–114, doi:10.1111/maps.12030.

[12] Reimold, W.U.; Crósta, A.P.; Hasch, M.; Kowitz, A.; Hauser, N.; Sanchez, J.P.; Simões, L.S.A.; de Oliveira, G.J.; Zaag, P.T. Shock Deformation Confirms the Impact Origin for the Cerro do Jarau, Rio Grande do Sul, Brazil, Structure. *Meteorit. Planet. Sci.* **2019**, *54*, 2384–2397, doi:10.1111/maps.13233.

[13] Reimold, W.U.; Koeberl, C. Impact Structures in Africa: A review. *J. Afr. Earth Sci.* **2014**, *93*, 57–175, doi:10.1016/j.jafrearsci.2014.01.008.

[14] Gratz, A. Deformation in Laboratory-Shocked Quartz. *J. Non Cryst. Solids* **1984**, *67*, 543–558, doi:10.1016/0022-3093(84)90175-3.

[15] Kowitz, A.; Güldemeister, N.; Schmitt, R.T.; Reimold, W.U.; Wünnemann, K.; Holzwarth, A. Revision and Recalibration of Existing Shock Classifications for Quartzose Rocks Using Low-Shock Pressure (2.5–20 GP a) Recovery Experiments and Mesoscale Numerical Modeling. *Meteorit. Planet. Sci.* **2016**, *51*, 1741–1761, doi:10.1111/maps.12712.

[16] Buchanan, P.; Reimold, W. Planar Deformation Features and Impact Glass in Inclusions from the Vredefort Granophyre, South Africa. *Meteorit. Planet. Sci.* **2002**, *37*, 807–822, doi:10.1111/j.1945-5100.2002.tb00857.x.

[17] Goltrant, O.; Cordier, P.; Doukhan, J.-C. Planar Deformation Features in Shocked Quartz; A Transmission Electron Microscopy Investigation. *Earth Planet. Sci. Lett.* **1991**, *106*, 103–115, doi:10.1016/0012-821X(91)90066-Q.

[18] Christie, J.; Ardell, A. Substructures of Deformation Lamellae in Quartz. *Geology* **1974**, *2*, 405–408, doi:10.1130/0091-7613(1974)2<405:SODLIQ>2.0.CO;2.

[19] Gratz, A.J.; Fisler, D.K.; Bohor, B.F. Distinguishing Shocked from Tectonically Deformed Quartz by the Use of the Sem and Chemical Etching. *Earth Planet. Sci. Lett.* **1996**, *142*, 513–521, doi:10.1016/0012-821X(96)00099-4.

[20] Gratz, A.J.; Tyburczy, J.; Christie, J.; Ahrens, T.; Pongratz, P. Shock Metamorphism of Deformed Quartz. *Phys. Chem. Miner.* **1988**, *16*, 221–233, doi:10.1007/BF00220689.

[21] Hamers, M.; Drury, M. Scanning Electron Microscope-Cathodoluminescence (SEM-CL) Imaging of Planar Deformation Features and Tectonic Deformation Lamellae in Quartz. *Meteorit. Planet. Sci.* **2011**, *46*, 1814–1831, doi:10.1111/j.1945-5100.2011.01295.x.

[22] Stöffler, D.; Gault, D.; Wedekind, J.; Polkowski, G. Experimental Hypervelocity Impact into Quartz Sand: Distribution and Shock Metamorphism of Ejecta. *J. Geophys. Res.* **1975**, *80*, 4062–4077, doi:10.1029/JB080i029p04062.

[23] Stöffler, D.; Langenhorst, F. Shock Metamorphism of Quartz in Nature and Experiment: I. Basic Observation and Theory. *Meteoritics* **1994**, *29*, 155–181, doi:10.1111/j.1945-5100.1994.tb00670.x.

[24] Vernooij, M.G.; Langenhorst, F. Experimental Reproduction of Tectonic Deformation Lamellae in Quartz and Comparison to Shock-Induced Planar Deformation Features. *Meteorit. Planet. Sci.* **2005**, *40*, 1353–1361, doi:10.1111/j.1945-5100.2005.tb00406.x.

[25] Langenhorst, F. Shock Metamorphism of Some Minerals: Basic Introduction and Microstructural Observations. *Bull. Czech Geol. Surv.* **2002**, *77*, 265–282.

[26] Ernstson, K.; Mayer, W.; Neumair, A.; Rappenglück, B.; Sudhaus, D. The Chiemgau Crater Strewn Field: Evidence of a Holocene Large Impact Event in Southeast Bavaria, Germany. *J. Sib. Fed* **2010**, *3*, 72–103.

[27] Ferriere, L.; Osinski, G.R. Shock Metamorphism. In *Impact Cratering: Processes and Products*, Osinski, G.R., Pierazzo, E., Eds.; John Wiley & Sons, New Jersey, 2012; pp. 106–124.

[28] Christie, J.; Griggs, D.; Carter, N. Experimental Evidence of Basal Slip in Quartz. *J. Geol.* **1964**, *72*, 734–756.

[29] Christie, J.M.; Raleigh, C.B. The Origin of Deformation Lamellae in Quartz. *Am. J. Sci.* **1959**, *257*, 385–407, doi:10.2475/ajs.257.6.385.

[30] McLaren, A.; Retchford, J.; Griggs, D.; Christie, J. Transmission Electron Microscope Study of Brazil Twins and Dislocations Experimentally Produced in Natural Quartz. *Phys. Status Solidi B* **1967**, *19*, 631–644, doi:10.1002/pssb.19670190216.

[31] McLaren, A.; Turner, R.; Boland, J.; Hobbs, B. Dislocation Structure of the Deformation Lamellae in Synthetic Quartz; A Study by Electron and Optical Microscopy. *Contrib. Mineral. Petrol.* **1970**, *29*, 104–115, doi:10.1007/BF00392018.

[32] Kieffer, S.W. Shock Metamorphism of the Coconino Sandstone at Meteor Crater, Arizona. *J. Geophys. Res.* **1971**, *76*, 5449–5473, doi:10.1029/JB076i023p05449.

[33] Kieffer, S.W.; Phakey, P.P.; Christie, J.M. Shock Processes in Porous Quartzite: Transmission Electron Microscope Observations and Theory. *Contrib. Mineral. Petrol.* **1976**, *59*, 41–93, doi:10.1007/BF00375110.

[34] Ernstson, K. Evidence of Meteorite Impact-Induced Thermal Shock in Quartz. In *Proceedings of the Modern Problems of Theoretical, Experimental, and Applied Mineralogy, Syktyvkar, Russia, 2020*, p. 1423.

[35] Ernstson, K.; Bauer, F.; Hiltl, M. A Prominent Iron Silicides Strewn Field and Its Relation to the Bronze Age/Iron Age Chiemgau Meteorite Impact Event (Germany). *Earth Sci.* **2023**, *12*, 26–40, doi:10.11648/j.earth.20231201.14.

[36] Ernstson, K.; Sideris, C.; Liritzis, I.; Neumair, A. The Chiemgau Meteorite Impact Signature of the Stöttham Archaeological Site (Southeast Germany). *Mediterr. Archaeol. Archaeomet.* **2012**, *12*, 249–259.

[37] Ernstson, K. Meteorite Impact Spallation: From Mega- to Micro-Scale. Available online: http://www.impact-structures.com/impact-educational/meteorite-impact-spallation-from-mega-to-micro-scale/ (accessed on 3 May 2023).

[38] Stöffler, D. Glasses Formed by Hypervelocity Impact. *J. Non-Cryst. Solids* **1984**, *67*, 465–502, doi:10.1016/0022-3093(84)90171-6.

[39] Stöffler, D.; Grieve, R. Metamorphic Rocks: A Classification and Glossary of Terms, Recommendation of the International Union of Geological Sciences, 2007.

[40] Wenk, H.-R.; Chandler, B.C.; Chen, K.; Li, Y.; Tamura, N.; Yu, R. Residual Lattice Strain in Quartzites as a Potential Palaeo-Piezometer. *Geophys. J. Int.* **2020**, *222*, 1363–1378, doi:10.1093/gji/ggaa226.

[41] Wenk, H.-R.; Janssen, C.; Kenkmann, T.; Dresen, G. Mechanical Twinning in Quartz: Shock Experiments, Impact, Pseudotachylites and Fault Breccias. *Tectonophysics* **2011**, *510*, 69–79, doi:10.1016/j.tecto.2011.06.016.

[42] Wenk, H.-R.; Lonardelli, I.; Vogel, S.; Tullis, J. Dauphiné Twinning as Evidence for an Impact Origin of Preferred Orientation in Quartzite: An Example from Vredefort, South Africa. *Geology* **2005**, *33*, 273–276, doi:10.1130/G21163.1.

[43] Wenk, H.-R.; Yu, R.; Vogel, S.; Vasin, R. Preferred Orientation of Quartz in Metamorphic Rocks from the Bergell Alps. *Minerals* **2019**, *9*, 277, doi:10.3390/min9050277.

[44] Barber, D.; Wenk, H.-R. Dauphiné Twinning in Deformed Quartzites: Implications of an in situ TEM Study of the α-β Phase Transformation. *Phys. Chem. Miner.* **1991**, *17*, 492–502, doi:10.1007/BF00202229.

[45] Houser, L.; Ault, A.; Newell, D.; Evans, J.; Shen, F.A.; Van Devener, B. Nanoscale Textural and Chemical Evolution of Silica Fault Mirrors in the Wasatch Fault Damage Zone, Utah, USA. *Geochem. Geophys. Geosyst.* **2021**, *22*, e2020GC009368, doi:10.1029/2020GC009368.

[46] Kowitz, A.; Güldemeister, N.; Reimold, W.; Schmitt, R.; Wünnemann, K. Diaplectic Quartz Glass and SiO2 Melt Experimentally Generated at Only 5 GPa Shock Pressure in Porous Sandstone: Laboratory Observations and Meso-Scale Numerical Modeling. *Earth Planet. Sci. Lett.* **2013**, *384*, 17–26, doi:10.1016/j.epsl.2013.09.021.

[47] Sharp, N.; McDonough, W.F.; Ticknor, B.W.; Ash, R.D.; Piccoli, P.M.; Borg, D.T. Rapid Analysis of Trinitite with Nuclear Forensic Applications for Post-Detonation Material Analyses. *J. Radioanal. Nucl. Chem.* **2014**, *302*, 57–67, doi:10.1007/s10967-014-3285-9.

[48] Donohue, P.H.; Simonetti, A. Vesicle Size Distribution as a Novel Nuclear Forensics Tool. *PLoS One* **2016**, *11*, e0163516, doi:10.1371/journal.pone.0163516.

[49] Day, J.M.; Moynier, F.; Meshik, A.P.; Pradivtseva, O.V.; Petit, D.R. Evaporative Fractionation of Zinc During the First Nuclear Detonation. *Sci. Adv.* **2017**, *3*, e1602668, doi:10.1126/sciadv.1602668.

[50] Bindi, L.; Kolb, W.; Eby, G.N.; Asimow, P.D.; Wallace, T.C.; Steinhardt, P.J. Accidental Synthesis of a Previously Unknown Quasicrystal in the First Atomic Bomb Test. *Proc. Nat. Acad. Sci. U S A.* **2021**, *118*, e2101350118, doi:10.1073/pnas.2101350118.

[51] Bunch, T.E. A Study of Shock-Induced Microstructures and Solid State Transformations of Several Minerals from Explosion Craters. University of Pittsburgh, Pittsburgh, 1966.

[52] Selby, H.D.; Hanson, S.K.; Meininger, D.; Oldham, W.J.; Kinman, W.S.; Miller, J.L.; Reilly, S.D.; Wende, A.M.; Berger, J.L.; Inglis, J; et al. A New Yield Assessment for the Trinity Nuclear Test, 75 Years Later. *Nucl. Technol.* **2021**, *207*, 321–325, doi:10.1080/00295450.2021.1932176.

[53] Hermes, R.E.; Strickfaden, W.B. A New Look at Trinitite. *Nucl. Weap. J.* **2005**, *2*, 2–7.

[54] Bunch, T.E.; Hermes, R.E.; Moore, A.M.; Kennett, D.J.; Weaver, J.C.; Wittke, J.H.; DeCarli, P.S.; Bischoff, J.L.; Hillman, G.C.; Howard, G.A; et al. Very High-Temperature Impact Melt Products as Evidence for Cosmic Airbursts and Impacts 12,900 Years Ago. *Proc. Nat. Acad. Sci. U S A.* **2012**, *109*, E1903–E1912, doi:10.1073/pnas.1204453109.

[55] Blenkinsop, T. Shock-induced microstructures and shock metamorphism. *Deformation Microstructures and Mechanisms in Minerals and Rocks*, 2000; pp. 80–89, doi:10.1007/0-306-47543-X.

[56] Bohor, B.; Betterton, W.; Krogh, T. Impact-Shocked Zircons: Discovery of Shock-Induced Textures Reflecting Increasing Degrees of Shock Metamorphism. *Earth Planet. Sci. Lett.* **1993**, *119*, 419–424, doi:10.1016/0012-821X(93)90149-4.

[57] Madden, M.E.E.; Kring, D.A.; Bodnar, R.J. Shock Reequilibration of Fluid Inclusions in Coconino Sandstone from Meteor Crater, Arizona. *Earth Planet. Sci. Lett.* **2006**, *241*, 32–46, doi:10.1016/j.epsl.2005.10.008.

[58] Langenhorst, F. Shock Experiments on Pre-Heated α-and β-Quartz: II. X-ray and TEM Investigations. *Earth Planet. Sci. Lett.* **1994**, *128*, 683–698, doi:10.1016/0012-821X(94)90179-1.

[59] Hamers, M.F.; Pennock, G.M.; Herwegh, M.; Drury, M.R. Distinction between Amorphous and Healed Planar Deformation Features in Shocked Quartz Using Composite Color Scanning Electron Microscope Cathodoluminescence (Sem-Cl) Imaging. *Meteorit. Planet. Sci.* **2016**, *51*, 1914–1931, doi:10.1111/maps.12711.

[60] MST. [ED] Electron Diffraction-Quartz Glass. Available online: https://www.mst.or.jp/Portals/0/en/en_ed.html (accessed on 3 December 2022).

[61] Gleason, A.; Bolme, C.; Lee, H.; Nagler, B.; Galtier, E.; Kraus, R.; Sandberg, R.; Yang, W.; Langenhorst, F.; Mao, W. Time-Resolved Diffraction of Shock-Released SiO2 and Diaplectic Glass Formation. *Nat. Commun.* **2017**, *8*, 1–6, doi:10.1038/s41467-017-01791-y.

[62] Eckert, J.; Gourdon, O.; Jacob, D.E.; Meral, C.; Monteiro, P.J.; Vogel, S.C.; Wirth, R.; Wenk, H.-R. Ordering of Water in Opals with Different Microstructures. *Eur. J. Mineral.* **2015**, *27*, 203–213, doi:10.1127/ejm/2015/0027-2428.

[63] Hamers, M.; Pennock, G.; Drury, M. Scanning Electron Microscope Cathodoluminescence Imaging of Subgrain Boundaries, Twins and Planar Deformation Features in Quartz. *Phys. Chem. Miner.* **2017**, *44*, 263–275, doi:10.1007/s00269-016-0858-x.

[64] Hamers, M.F. Identifying Shock Microstructures in Quartz from Terrestrial Impacts: New Scanning Electron Microscopy Methods. UU Department of Earth Sciences, 2013.

[65] Kalceff, M.A.S.; Phillips, M.R.; Moon, A.R.; Kalceff, W. Cathodoluminescence Microcharacterisation of Silicon Dioxide Polymorphs. In *Cathodoluminescence in Geosciences*; Springer, 2000; pp. 193–224.

[66] French, B.M. Traces of Catastrophe: A Handbook of Shock-Metamorphic Effects in Terrestrial Meteorite Impact Structures; Lunar and Planetary Institute: Washington DC, 1998.

[67] Schubnikow, A.; Zinserling, K. Über die Schlag-und Druckfiguren und über die mechanischen Quarzzwillinge. *Z. Kristallogr. Cryst. Mat.* **1932**, *83*, 243–264, doi:10.1524/zkri.1932.83.1.243.

[68] Tullis, J. Quartz: Preferred Orientation in Rocks Produced by Dauphiné Twinning. *Science* **1970**, *168*, 1342–1344, doi:10.1126/science.168.3937.1342.

[69] Hacker, B.R.; Abers, G.A. Subduction Factory 3: An Excel Worksheet and Macro for Calculating the Densities, Seismic Wave Speeds, and H2O Contents of Minerals and Rocks at Pressure and Temperature. *Geochem. Geophys. Geosyst.* **2004**, *5*, doi:10.1029/2003GC000614.

[70] Chao, E.; Fahey, J.; Littler, J.; Milton, D. Stishovite, SiO2, a Very High Pressure New Mineral from Meteor Crater, Arizona. *J. Geophys. Res.* **1962**, *67*, 419–421, doi:10.1029/JZ067i001p00419.

[71] El Goresy, A.; Dubrovinsky, L.; Sharp, T.G.; Chen, M. Stishovite and Post-Stishovite Polymorphs of Silica in the Shergotty Meteorite: Their Nature, Petrographic Settings Versus Theoretical Predictions and Relevance to Earth's Mantle. *J. Phys. Chem. Solids* **2004**, *65*, 1597–1608, doi:10.1016/j.jpcs.2004.02.001.

[72] Martini, J. Coesite and Stishovite in the Vredefort dome, South Africa. *Nature* **1978**, *272*, 715–717, doi:10.1038/272715a0.

[73] Fahey, J. Recovery of Coesite and Stishovite from Coconino Sandstone of Meteor Crater, Arizona. *Am. Mineral.* **1964**, *49*, 1643–1647.

[74] Melosh, H.J. Impact Cratering: A Geologic Process; Oxford University Press; Oxford: Clarendon Press: New York, 1989.

[75] Ernstson, K.; Poßekel, J. Enigmatic Meteorite Impact Signature: Field Evidence and Ground Penetrating Radar (GPR) Measurements Suggest Megascopic Impact Spallation Features. In *Proceedings of the AGU Fall Meeting Abstracts*, 2019; pp. EP53F-2239.

[76] Ernstson, K.; Schulz-Hertlein, G.; Ernstson, T.; Poßekel, J. A Probable Holocene Meteorite Impact Crater Strewn Field in Lower Franconia (Germany): Evidence from Digital Terrain Models and Geophysical Surveys (GPR, Electrical Imaging, Geomagnetics). In *Proceedings of the Fall Meeting 2022*, 2022.
[77] Glasstone, S.; Dolan, P.J. *The Effects of Nuclear Weapons*, 3rd ed.; US Dept of Defense, U.S. Government Printing Office: Washington, DC, 1977.
[78] Kenkmann, T.; Hornemann, U.; Stöffler, D. Experimental Generation of Shock-Induced Pseudotachylites Along Lithological Interfaces. *Meteorit. Planet. Sci.* **2000**, *35*, 1275–1290, doi:10.1111/j.1945-5100.2000.tb01516.x.
[79] Martinelli, G.; Plescia, P.; Tempesta, E.; Paris, E.; Gallucci, F. Fracture Analysis of α-Quartz Crystals Subjected to Shear Stress. *Minerals* **2020**, *10*, 870, doi:10.3390/min10100870.
[80] Hermes, R.E.; Wenk, H.-R.; Kennett, J.P.; Bunch, T.E.; Moore, C.R.; LeCompte, M.A.; Kletetschka, G.; Adedeji, A.V.; Langworthy, K.; Razink, J.; et al. Microstructures in Shocked Quartz: Linking Nuclear Airbursts and Meteorite Impacts. *Preprints.org* **2023**, doi:10.20944/preprints202308.0221.v1.
[81] Ernstson, K. Pink Quartz-a New, Meteorite Impact-Related Origin? Part 1: Observations and First Hypothesis of Formation. Available online: http://www.impact-structures.com/2018/08/pink-quartz-a-new-meteorite-impact-related-origin-part-1-observations-and-first-hypothesis-of-formation/ (accessed on January 2023).
[82] Ernstson, K. Looking into the Cobbles. Available online: http://www.impact-structures.com/impact-spain/shock-deformation-in-triassic-buntsandstein-conglomerates-spain/looking-into-the-cobbles/ (accessed on January 2023).
[83] Moore, A.M.T.; Kennett, J.P.; LeCompte, M.; Moore, C.R.; Li, Y.-Q.; Kletetschka, G.K.; Langworthy, K.; Razink, J.J.; Brogden, V.; van Devener, B.; et al. Abu Hureyra, Syria, Part 1: Shock-Fractured Quartz Grains Support 12,800-Year-Old Cosmic Airburst at the Younger Dryas Onset. *ScienceOpen* **2023**, *1*.
[84] Demitroff, M.; LeCompte, M.; Rock, B. Cold Climate Related Structural Sinks Accommodate Unusual Soil Constituents, Pinelands National Reserve, New Jersey, USA. In *Proceedings of the AGU Fall Meeting Abstracts*, 2009; pp. PP31D-1394.
[85] Mahaney, W.; Kalm, V.; Krinsley, D.; Tricart, P.; Schwartz, S.; Dohm, J.; Kim, K.; Kapran, B.; Milner, M.; Beukens, R.; et al. Evidence from the Northwestern Venezuelan Andes for Extraterrestrial Impact: The Black Mat Enigma. *Geomorphology* **2010**, *116*, 48–57, doi:10.1016/j.geomorph.2009.10.007.
[86] Ernstson, K.; Poßekel, J.; Rappenglück, M.A. Near-Ground Airburst Cratering: Petrographic and Ground Penetrating Radar (GPR) Evidence for a Possibly Enlarged Chiemgau Impact Event (Bavaria, SE-Germany). In *Proceedings of the Lunar and Planetary Science Conference*, 2020; p. 1231.
[87] Bunch, T.E.; LeCompte, M.A.; Adedeji, A.V.; Wittke, J.H.; Burleigh, T.D.; Hermes, R.E.; Mooney, C.; Batchelor, D.; Wolbach, W.S.; Kathan, J.; et al. A Tunguska Sized Airburst Destroyed Tall el-Hammam a Middle Bronze Age City in the Jordan Valley nNear the Dead Sea. *Sci. Rep.* **2021**, *11*, 1–64, doi:10.1038/s41598-021-97778-3.

Appendices

Methods

Appendix: Samples

METEOR CRATER This sample was collected in 1966 by co-author T.E.B. on the rim ~500 m north of the crater's center at ~35.032206° N, 111.023988° W.

JOE-1/4 This sample was obtained in 2011 at the Semipalatinsk test site by Dr. Byron Ristvet, DTRA, with permission from the Kazakhstan National Nuclear Center and the Russian Federation Atomic Energy Agency. The bulk sample was sifted to obtain the fine sand studied.

TRINITY A sediment sample "JIE" was obtained in 2003 at the Trinity Site near ground zero by Jim Eckles of the White Sands Missile Range Public Affairs Office. The gross sample was sifted to remove fines as well as larger rocks. The resulting sand fraction was used to produce the thin-sectioned slides for this investigation. The "meltglass" sample was obtained in 2011 at the Trinity Site about 400 meters NNE from ground zero, where it landed following ejection by the detonation. Co-author R.E.H. collected it with permission from the White Sands Missile Range Public Affairs office, and part of it was thin-sectioned for this study.

Appendix: Processing steps

(i) Sediment was wet-sieved to concentrate grains between diameters of ~150 (#100 ASTM sieve) to ~850 μm (#20 ASTM sieve).
(ii) Typically, the sorted grains were treated with HCl to remove carbonates.
(iii) Grains were embedded in blue epoxy for better visibility, covering the entire 27 × 46 mm slide, and were sectioned at Spectrum Petrographics, Vancouver, WA. Sectioned slides were given a high-polish, microprobe-grade finish necessary for EBSD analyses. No cover slide was used.
(iv) Slides were etched with HF vapor at 50% concentration for ~2 min. Note that exposure for <2 min was insufficient for etching and exposing shock fractures; exposure for >2 min can damage the slides.
(v) Grains were examined using a petrographic polarizing microscope with a rotary stage. The microscope was equipped with transmitted light and epi-illumination (reflected light). First, epi-illumination was used, and then transmitted light was used with objectives ranging from 04× to 100× magnification. Once a candidate grain was identified, it was rotated to extinction under cross polars. Photomicrographs were acquired under both transmitted light and epi-illumination.
(vi) SEM imaging was performed after re-polishing the etched grains to a microprobe finish using 50 nm colloidal silica.
(vii) Next, the elemental compositions of individual grains were determined using SEM-based EDS.
(viii) Cathodoluminescence was recorded in both panchromatic (185–850 nm wavelengths) and 3-filtered (RGB) formats. Because red, green, and blue channels were optimized individually to obtain the maximum

amount of information from the image, color information in the images is non-quantitative.

(ix) EBSD analyses were performed using multiple routines.

(x) FIB foils were extracted from selected quartz grains.

(xi) TEM analyses were performed on individual foils.

(xii) Elemental compositions of the grains were determined using TEM-based EDS. FFTs and bi-plots of d-spacing and intensity were produced with Digital Micrograph, version 3.32.2403.0. Because electron microscopy is capable of causing irradiation-induced amorphization [23], quartz grains were examined at low magnification using low voltages and short image-acquisition times.

Appendix: Analytical details

HF etching Following Bunch et al. [87], Spectrum Petrographics, Vancouver, WA, etched thin-sectioned slides by exposure to HF vapor for 2 min to dissolve amorphous quartz and make any lamellae more visible. After treatment with HF vapor, we performed another dH_2O rinse.

Alternately, we treated some slides with liquid HF for 2 min, after which we performed a dH_2O rinse; neutralized them with 5% sodium carbonate solution; rinsed them with dH_2O again; and then treated them with 5% HCl to remove carbonates. The HF vapor produced more consistent results than liquid HF. Multiple studies [9, 14, 19, 21, 55, 56] have demonstrated the utility of etching quartz grains with HF to differentiate between glass-filled shock features and glass-free tectonic deformation lamellae. In our study, we observed that HF sometimes lightly etches tectonic deformation lamellae to reveal broad, shallow depressions, as others reported [9, 55]. However, unlike shock fractures, these depressions in the damaged lattice did not extend more than a few microns into the grain and were not observed to contain amorphous silica.

Optical transmission microscopy (OPT) For this study, we made polished thin sections of quartz grains and meltglass to search for potentially shocked quartz grains at three sites. For Meteor Crater, 36 quartz grains were analyzed at concentrations of 600 grains/cm^2 (Appendix, Figure S1); for the Joe-1/4 site, 24 grains at 150/cm^2 (Appendix, Figure S2) and for Trinity, 42 grains at 700/cm^2 (Appendix, Figure S3). **Epi-illumination microscopy (EPI).** This optical technique uses reflected light to image the surfaces of the grains investigated.

SEM and SEM-EDS Dark-field STEM images were acquired on focused ion beam foils. Standard practices were used for STEM analyses. At Elizabeth City State University, North Carolina, analyses were conducted in low-vacuum mode using a JEOL-6000 SEM system. At the University of Oregon, we used a ThermoFisher Apreo 2 SEM with a CL detector. Using SEM-EDS, we manually selected for detection of major elements with uncertainties of approximately ±10%. At the University of Utah, secondary and backscattered electron images were collected using a Teneo SEM system (Thermofisher FEI, Hillsboro, OR).

TEM, STEM, and TEM-EDS At the CAMCOR facility at the University of Oregon, Transmission/Scanning transmission electron microscopy, or (S)TEM, was performed on an FEI 80–300 Titan scanning/transmission electron microscope (STEM) equipped with an image corrector, High-Angle Annular Dark Field (HAADF) detector, Energy Dispersive X-ray Spectroscopy (EDS) detector, Gatan Imaging Filter (GIF), and a 4-megapixel Charge-Coupled Device (CCD) camera. Microscope magnification was calibrated using a standard cross-grating carbon replica (2,160 lines/mm) evaporated with Au-Pd (Ted Pella #607). All images, diffraction patterns, and EDX maps were collected at 300 Kv and processed using Digital Micrograph, version 3.32.2403.0.

STEM/TEM was performed on a JEOL 2800 operated at 200 kV at the University of Utah. EDS data was collected and processed using ThermoFisher Noran System 7 software. Spectral maps were processed as net-counts (background subtracted) using a 5×5 kernel size. Quantitative results were obtained using the Cliff-Lorimer method with absorption correction.

Fast-Fourier transform (FFT) The diffraction characteristics of the FIB foils were investigated using FFT, an image processing technique for analyzing high-resolution TEM (HRTEM) images in reciprocal space. The FFT algorithm calculates the frequency distribution of pixel intensities in an HRTEM image, and then, any periodicity is displayed as spots in an output image, thus revealing the crystal's structure. HRTEM and FFT allow the measurement of interatomic spacings, known as d-spacings, measured in nm or angstroms (Å).

Focused ion beam This technique creates a thin specimen (avg: ~175 nanometers (nm) thick) by milling a quartz grain with focused gallium (Ga) ions. The resulting specimen, called a foil, is then analyzed using TEM. At the CAMCOR facility of the University of Oregon, TEM samples of quartz foils were prepared using a Helios Dual Beam SEM FIB. At the Surface Analysis Laboratory at the University of Utah, TEM sample preparation of quartz foils from bulk specimens was performed on an FEI/Thermo Helios Nanolab 650. The lift-out procedure followed standard sample preparation techniques. An electron beam deposited platinum layer as first locally deposited. Next, an ion-beam platinum layer was deposited. Trenches were milled on each side of the protective layer. Cuts were then made to the underside, and a micromanipulator probe was placed in contact with the surface (Omniprobe 200). The probe was attached by depositing platinum, and then the sample was cut free from the bulk. After using the micromanipulator probe, the lift-out was attached to a copper

support grid. The sample was then thinned using the ion beam at progressively decreasing accelerating voltages, 30 kV, 16 kV, 8 kV, and 2 kV.

Cathodoluminescence At the University of Oregon, cathodoluminescent (CL) images were synchronously captured at red (R), green (G), and blue (B) wavelengths on coated thin sections in low-vacuum mode on a Thermo Apreo2 S FE-SEM at 10 kV using 3.2 nA of beam current at ~10 mm working distance with 50Pa of chamber pressure to balance charge. Individual images using red, blue, and green wavelength filters on the CL detector were acquired and composited to create a 24-bit color image. Wavelength ranges: red: 595–813 nm; green: 495–615; and blue: 291–509 nm. Backscatter (BSE) and secondary (SE) electron images were captured with similar beam settings.

Electron backscatter diffraction (EBSD) EBSD is an SEM-based analytical technique in which an electron beam scans across a crystalline sample tilted at 70°. The diffracted electrons produce what are called Kikuchi patterns that reveal the microstructural properties of the sample.

At the University of California, Berkeley, SEM analyses were performed with a Zeiss EVO for imaging operated at 20 kV and EDS analyses used an EDAX-AMETEK spectrometer with corresponding Genesis software. EBSD mapping used a Digiview detector and TSL-OIM software. At the University of Utah, a Velocity Super EBSD camera (EDAX, Pleasanton, CA) was used to collect diffracted electrons for crystal structure analysis.

At the University of Utah, secondary and backscattered electron SEM images were collected using a Teneo system (Thermofisher FEI; Hillsboro, OR). EDS, EBSD, and CL analyses were similarly conducted with the same SEM system installed with the following detectors. An Octane Elite EDS system (EDAX, Pleasanton, CA) was used to collect elemental spectra. A Monarc CL Detector (Gatan; Pleasanton, CA) was used for cathodoluminescence studies. SEM beam energy and current were optimized to meet the requirements of each analysis mode. Before imaging, sample slides were polished to 0.20 µm roughness with colloidal silica suspension and washed with water to remove residues. The slides were then coated with 5-nm-thick carbon using a Leica EM ACE600 coater (Leica Microsystems, Inc., Deerfield, IL) to prevent charging during the imaging process.

Micro-Raman We investigated the shock fractures using micro-Raman with poor results. Even after highly polishing the quartz grains, their extensive fractures and amorphization made it challenging to acquire Raman spectra.

Universal stage We also investigated the shock fractures using the universal stage. However, we could not determine Miller indices because the observed shock fractures are non-planar and, thus, cannot be accurately measured and compared to planar features.

Image processing Most images were globally adjusted for balance, brightness, contrast, and sharpness, and some images were cropped to fit the space. A few images were rotated for clarity, and the legends and scale bars were repositioned at the bottom of the figures. Legends sometimes became unreadable for RGB images and some resized images, so they were replaced with the original, legible legend. EDS figures were composited from multiple printouts. No data within the figures were changed or obscured in making any adjustments.

Appendix: Figures

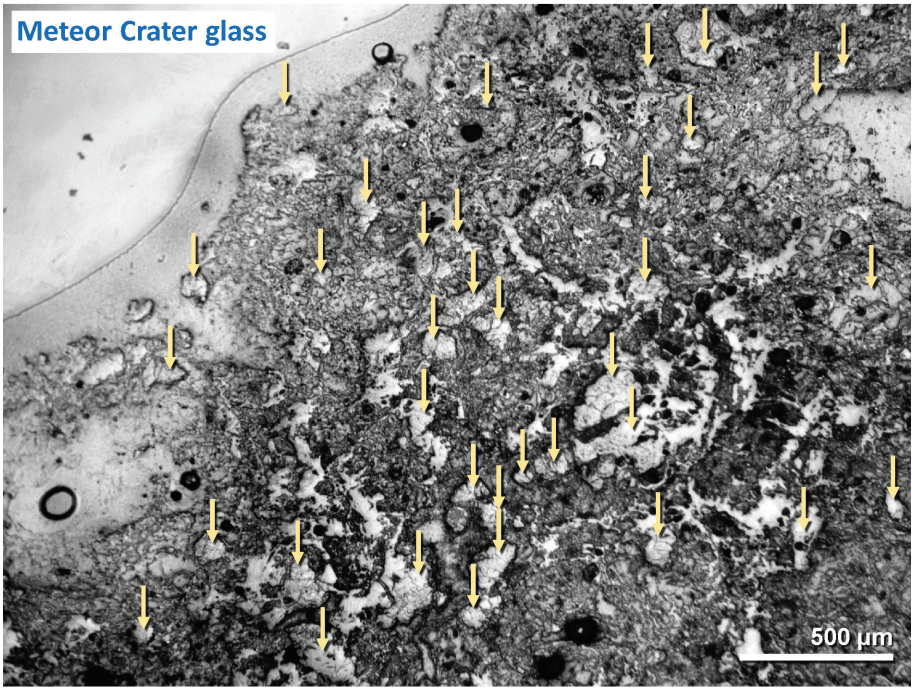

Figure S1: Meltglass containing shock-fractured quartz from Meteor Crater. Epi-photomicrograph of a thin-sectioned slide. We analyzed ~36 quartz grains (arrows) displaying shock fractures in a fragment of ejected meltglass. Shock-fractured grains were concentrated at ~600 quartz grains per cm^2.

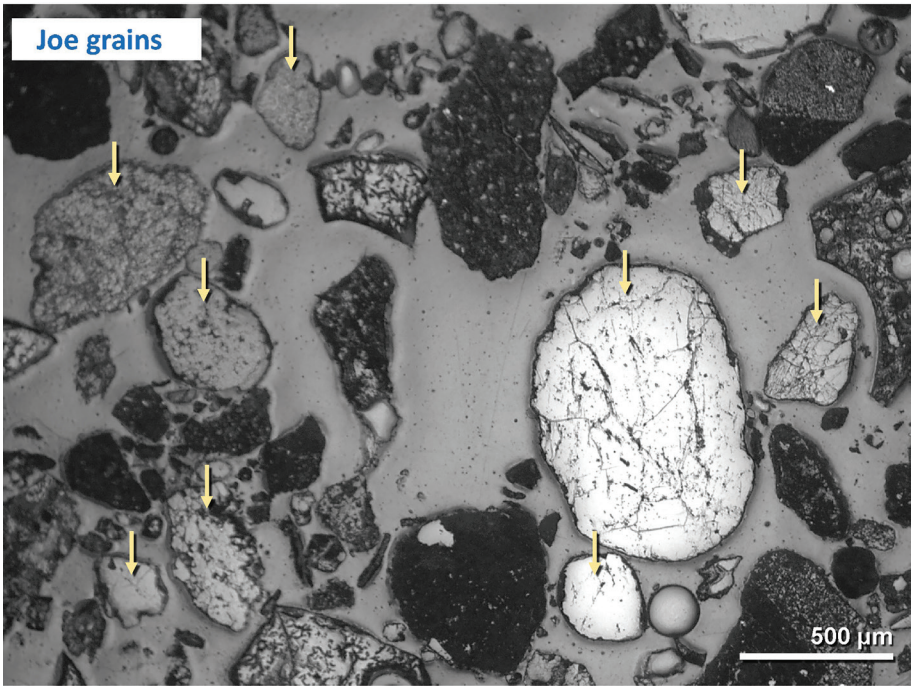

Figure S2: Shock-fractured quartz grains from the Joe-1/4 atomic test site. Epi-photomicrograph of a thin-sectioned slide. We analyzed ~24 loose grains (9 shown at arrows) with shock fractures. Extracted from test site sediment at a concentration of ~150 quartz grains per cm^2.

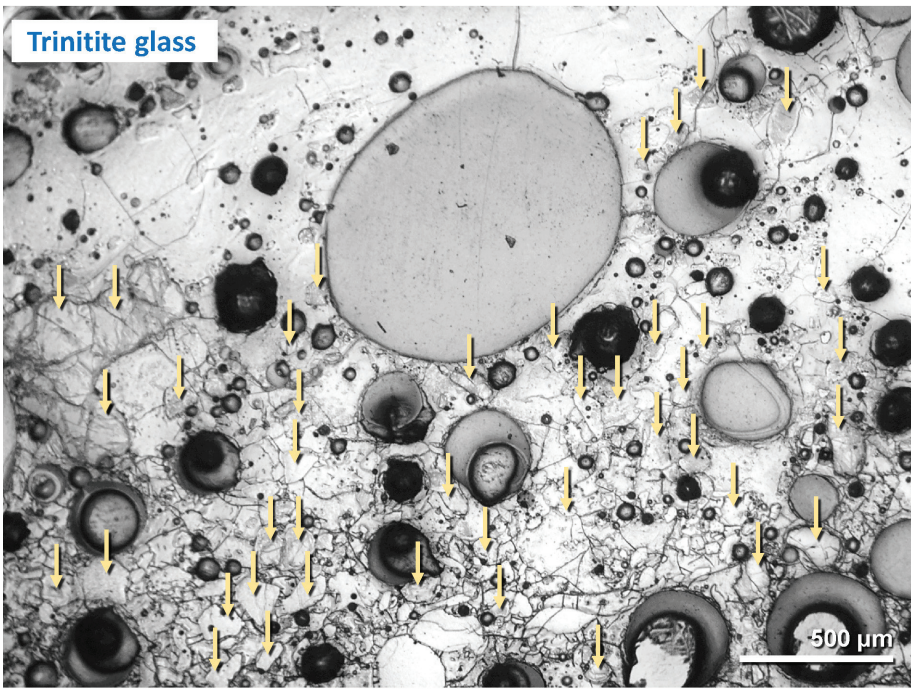

Figure S3: Shock-fractured quartz grains in Trinity meltglass. Epi-photomicrograph of a thin-sectioned slide. We analyzed 42 grains (arrows) with shock fractures from ejected meltglass at a concentration of ~700 quartz grains per cm^2.

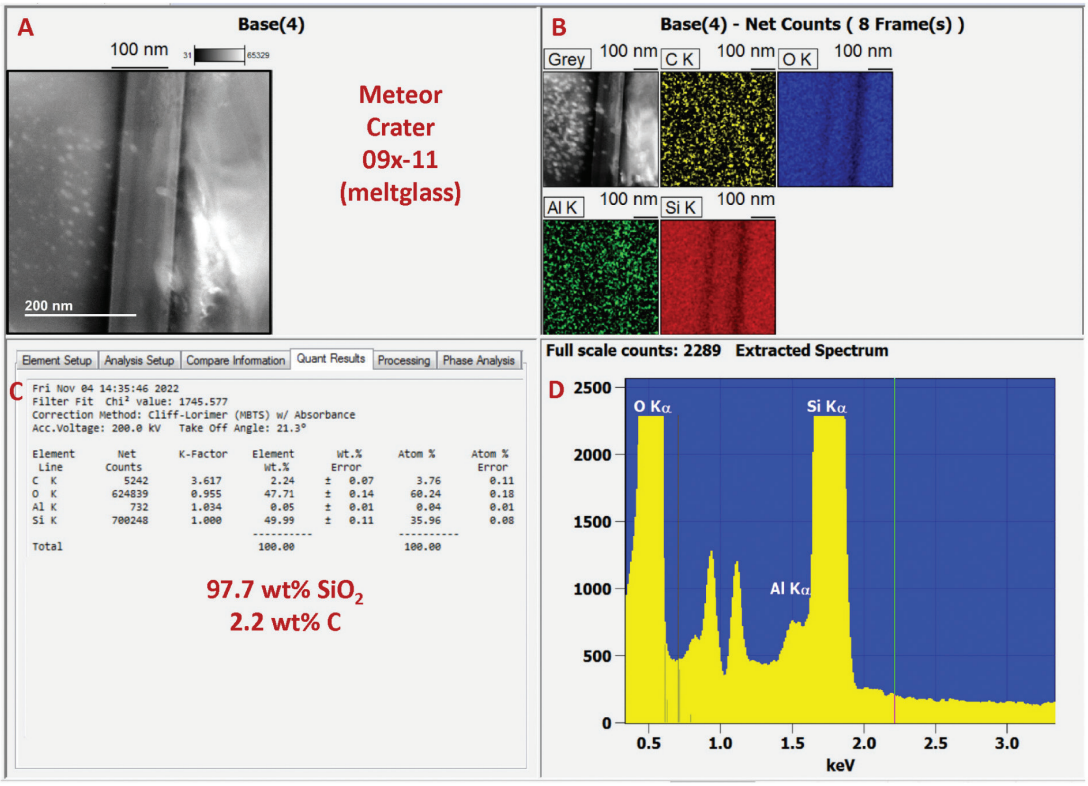

Figure S4: TEM-EDS data for Meteor Crater grain 09x-11. 97.7 wt% SiO_2, 2.2 wt% C, and 0.05 wt% Al. Note that the C and Al are distributed evenly across the foil, suggesting contamination from processing the sample. **(A)** TEM image showing area with amorphous silica (center) in the grain. EDS analyses were made on the entire field of view. **(B)** Panels showing concentrations of selected elements. **(C)** Elemental concentrations were measured for the entire field of view. **(D)** Energy spectrum for various elements of EDS analysis. These descriptions also apply to captions for Figures S7–S9 below.

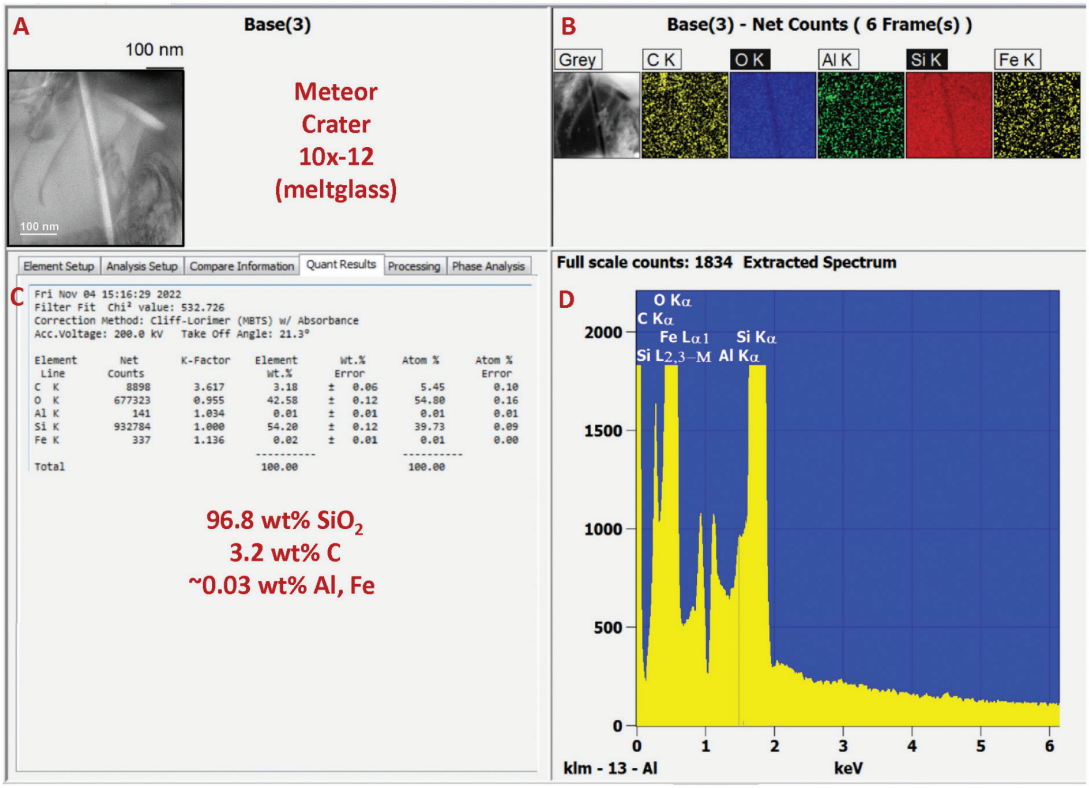

Figure S5: **TEM-EDS data for Meteor Crater grain 10x-12.** 96.8 wt% SiO_2, 3.2 wt% C, 0.02 wt% Fe, and 0.01 wt% Al. Note that the C, Fe, and Al appear to be contaminants introduced during the processing of the sample. For descriptions of panels, see the caption for Figure S6.

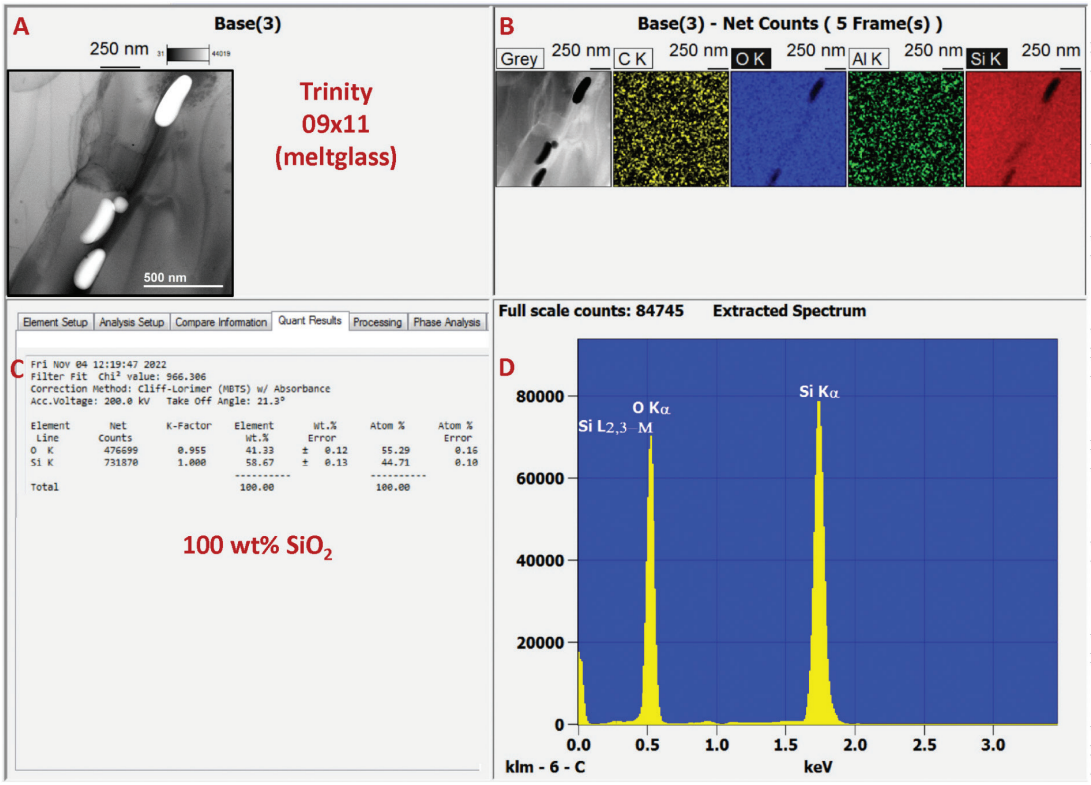

Figure S6: **TEM-EDS data for Trinity meltglass grain 09x11.** ~100 wt% SiO_2 with negligible amounts of Al and C, most likely contamination from processing the sample. For descriptions of panels, see the caption for Figure S6.

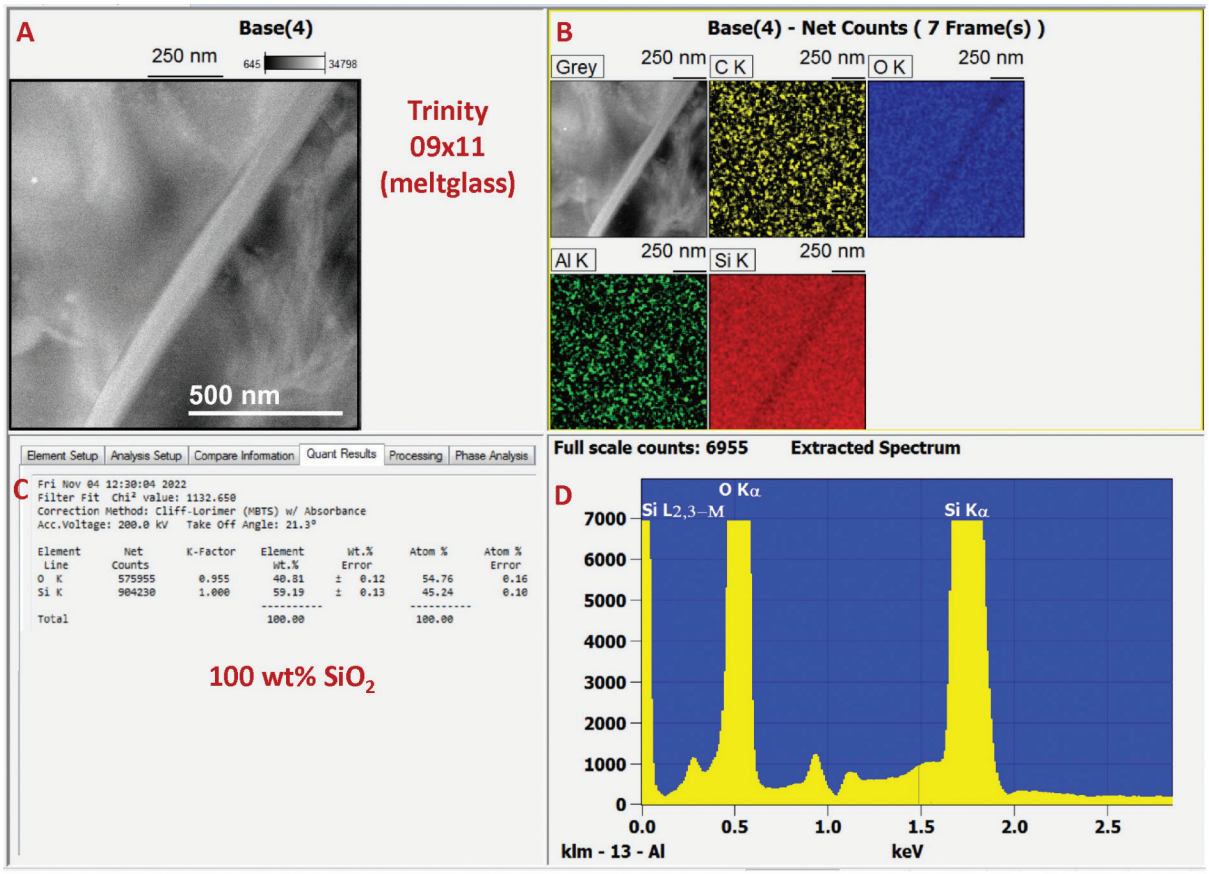

Figure S7: Additional TEM-EDS data for Trinity meltglass grain 09x11. ~100 wt% SiO_2 with insignificant amounts of Al and C, most likely contamination from processing the sample. For descriptions of panels, see the caption for Figure S6.

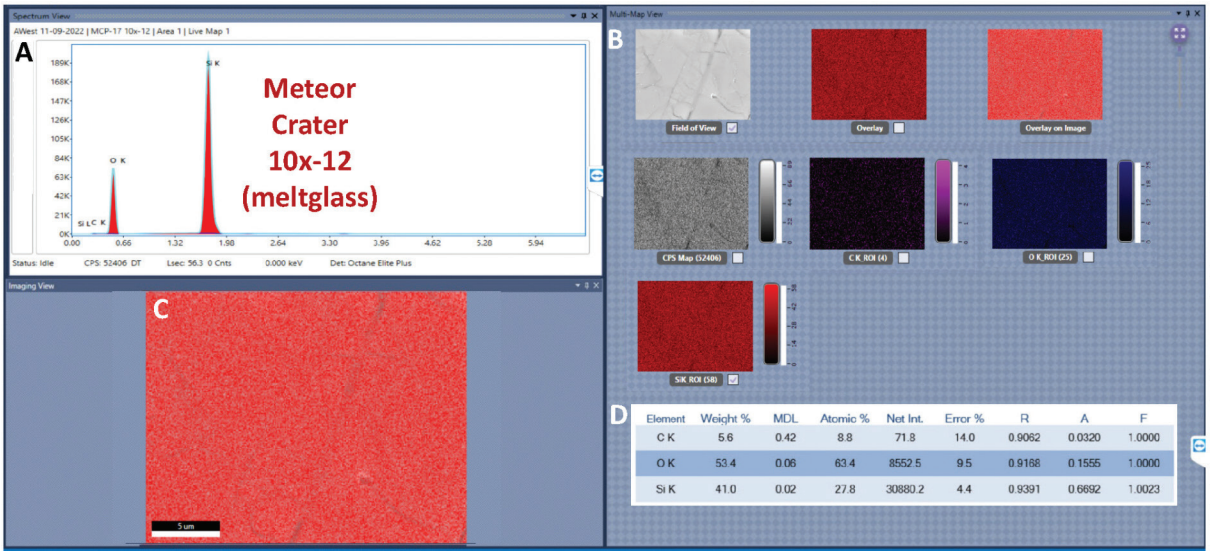

Figure S8: SEM-based EDS spectrum for Meteor crater grain 10x-12. (A) Energy spectrum for various elements of EDS analysis. EDS analyses were made on the entire field of view. **(B)** Panels showing concentrations of selected elements. **(C)** Composite image showing silicon panel overlying the SEM field of view. **(D)** Elemental concentrations were measured for the entire field of view. These descriptions also apply to captions for Figures S11–S14 below.

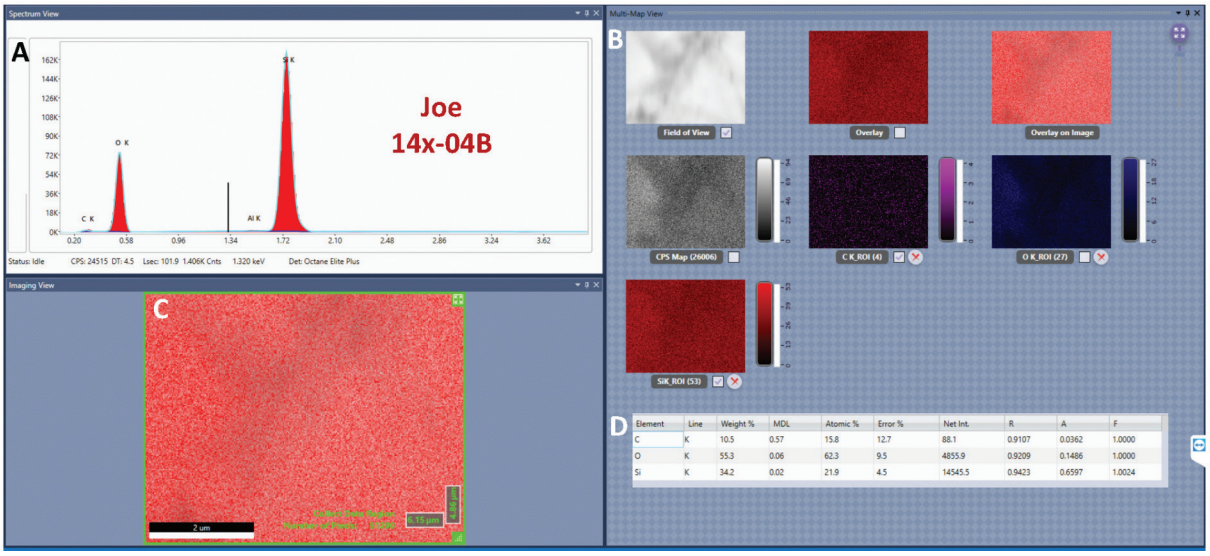

Figure S9: **SEM-based EDS spectrum for Joe-1/4 grain 14x-04B**. For descriptions of panels **(A)-(D)**, see the caption for Figure S10.

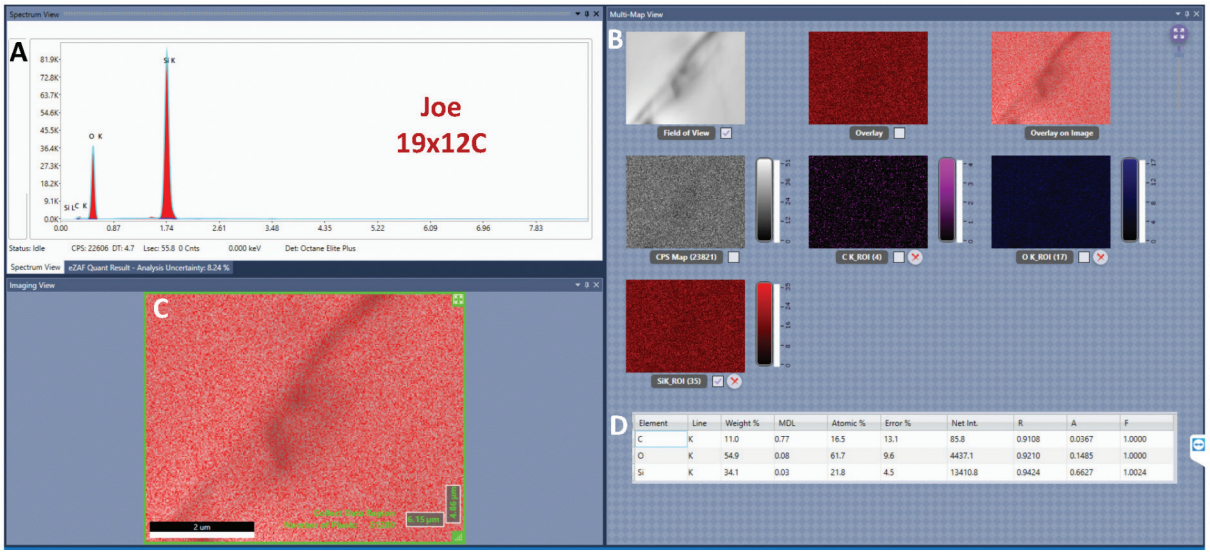

Figure S10: **SEM-based EDS spectrum for Joe-1/4 grain 19x-12C.** For descriptions of panels **(A)-(D)**, see the caption for Figure S10.

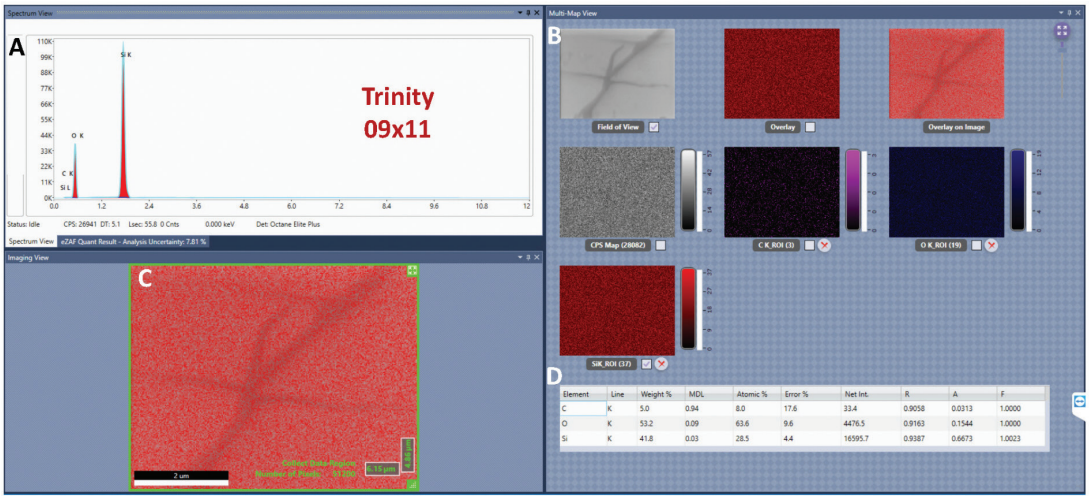

Figure S11: SEM-based EDS spectrum for Trinity meltglass grain 09x11. For descriptions of panels **(A)-(D)**, see the caption for Figure S10.

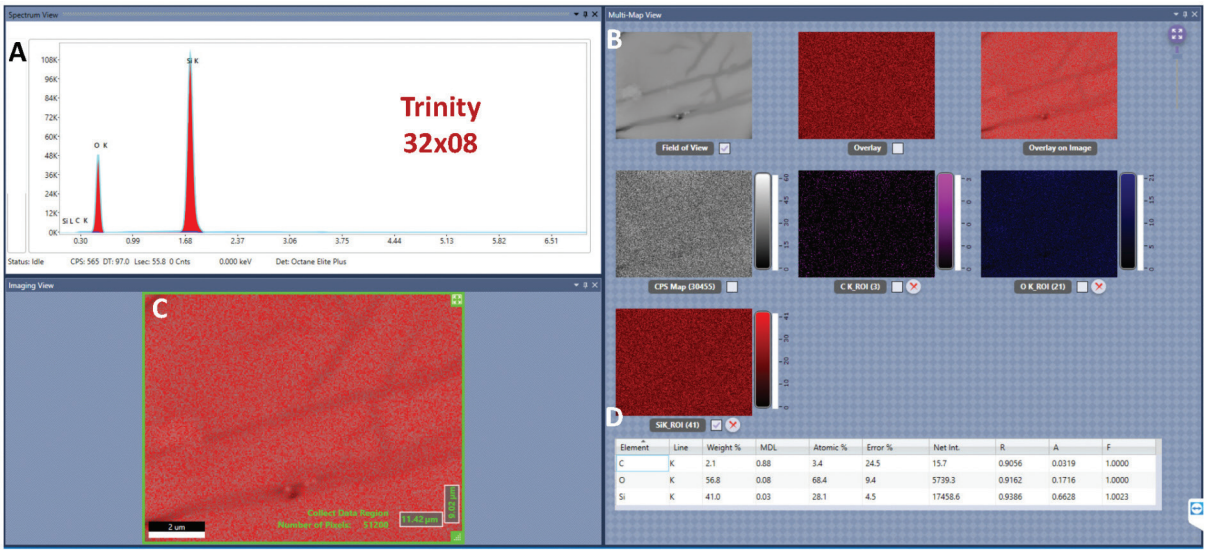

Figure S12: SEM-based EDS spectrum for Trinity meltglass grain 32x08. For descriptions of panels **(A)-(D)**, see the caption for Figure S10.

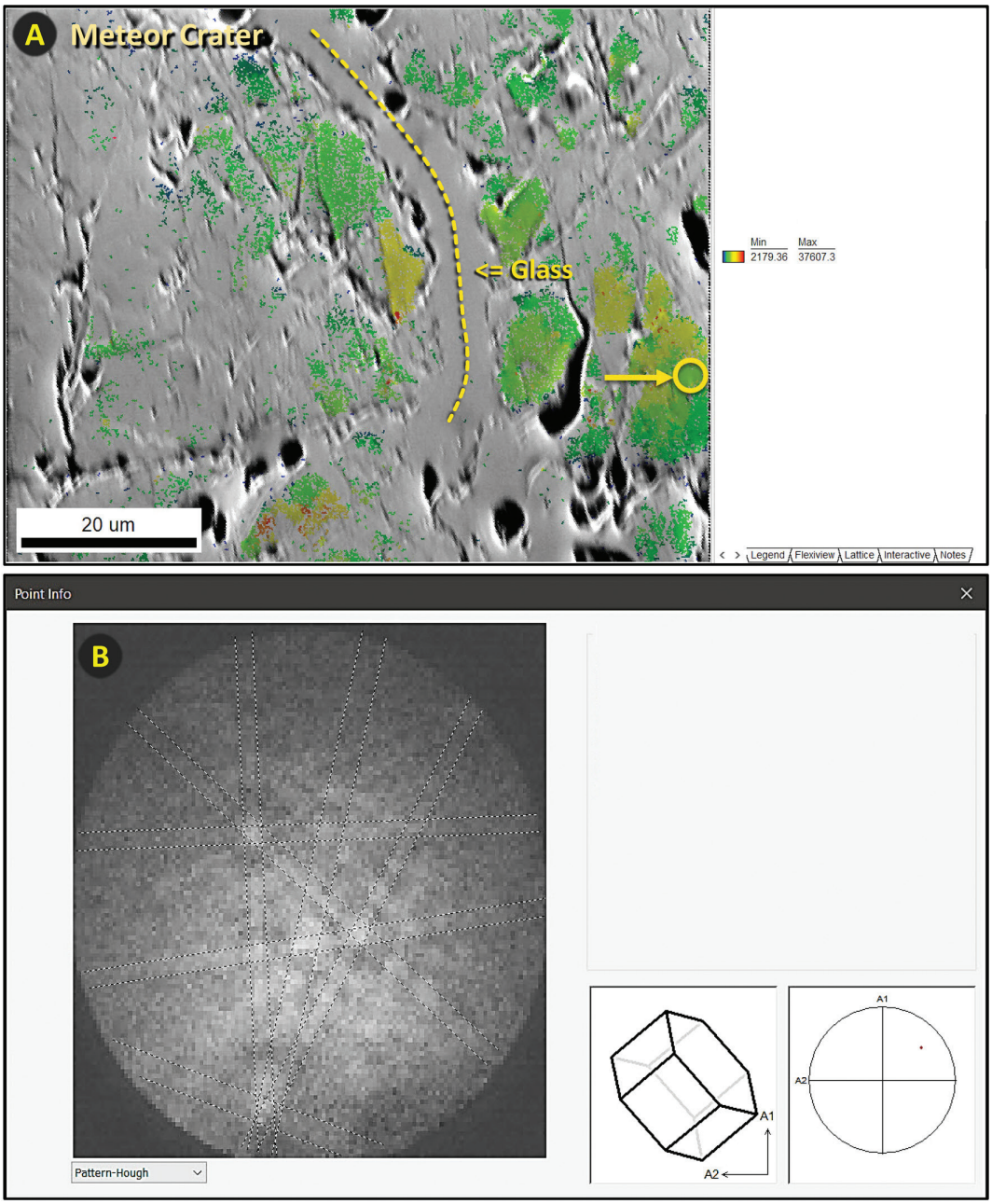

Figure S13: **EBSD Kikuchi patterns of shock-fractured quartz. (A)** Meteor Crater grain 10x-12. EBSD image of virtual backscatter results (similar to SEM-BSE image) overlain by the grain average image quality. Blue/green/yellow/red colors denote decreasing image quality. Gray color represents areas where no Kikuchi patterns were detected, suggesting the area is amorphous or has short-range ordering of crystals. The gray area along the dashed yellow line is interpreted as a region of amorphous silica that intruded into the grain or melted *in situ*. **(B)** For EBSD analyses, the diffracted electrons produce what are called Kikuchi patterns that reveal the microstructural properties of the sample. The panel shows an EBSD Kikuchi pattern from a spot in the yellow circle in panel **A**. The lattice diagram at the lower right represents the grain's crystalline structure in which the hexagonal surface is the basal plane (0001), with the c-axis perpendicular to it.

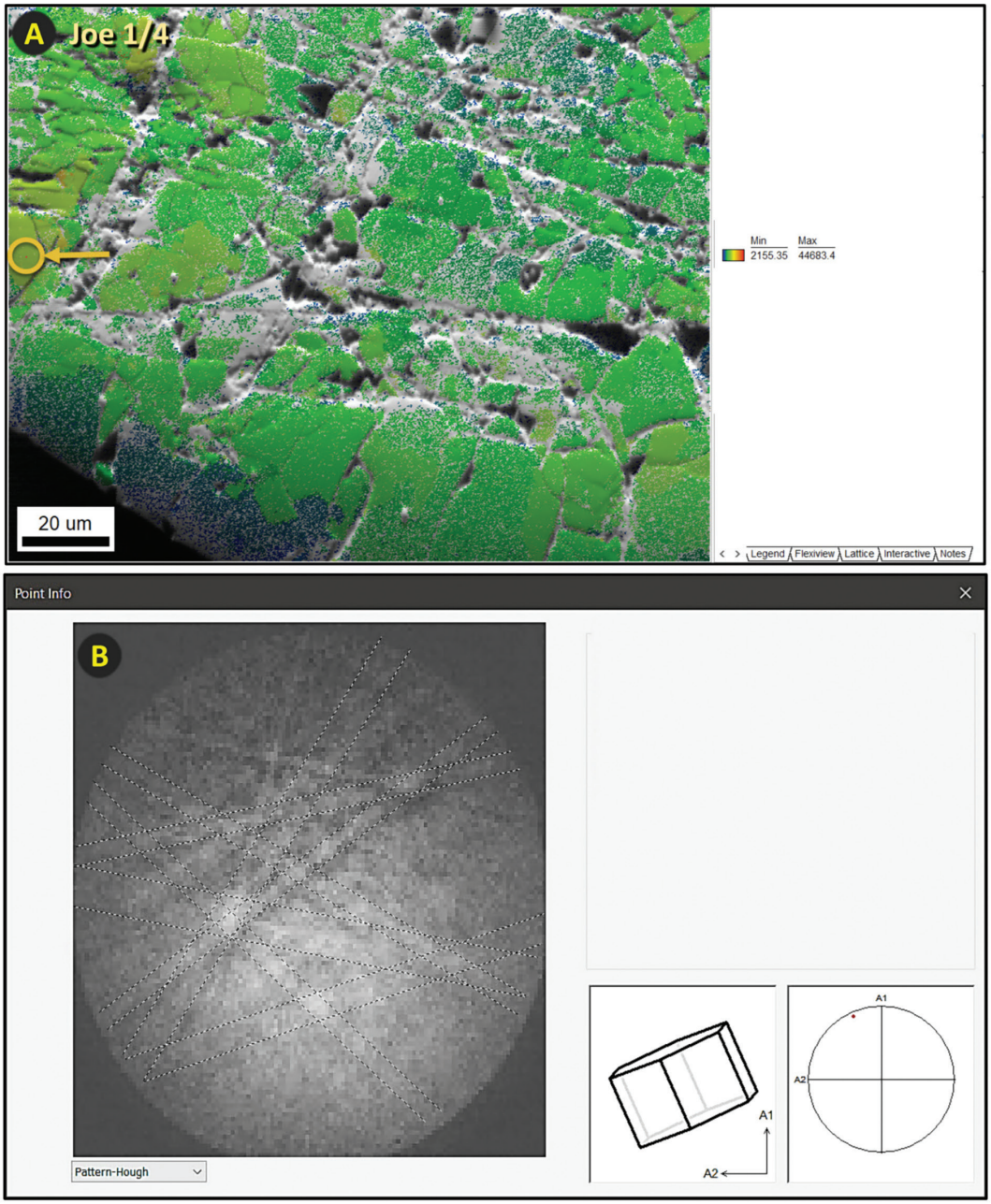

Figure S14: EBSD Kikuchi patterns of shock-fractured quartz. (A) Joe-1/4 grain 14x-04B. EBSD image of virtual backscatter results (similar to SEM-BSE image) overlain by the grain average image quality. Blue/green/yellow/red colors denote decreasing image quality. Gray color represents areas where no Kikuchi patterns were detected, suggesting the area is amorphous or has short-range ordering of crystals. **(B)** EBSD Kikuchi pattern from a spot in the yellow circle in panel **A**. The lattice diagram at the lower right represents the grain's crystalline structure in which the hexagonal surface is the basal plane (0001), with the c-axis perpendicular to it.

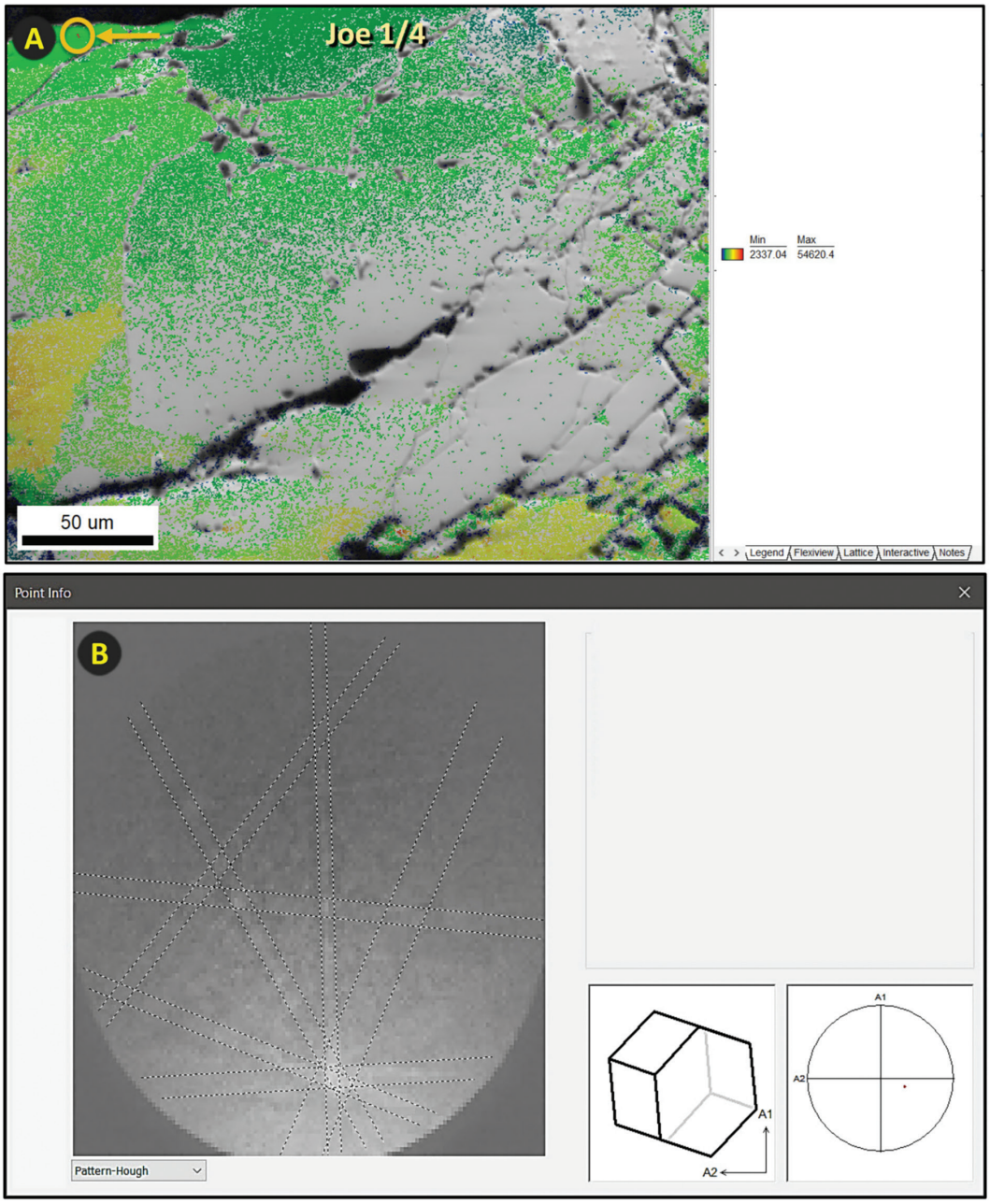

Figure S15: EBSD Kikuchi patterns of shock-fractured quartz. **(A)** Joe-1/4 grain 19x-12C. EBSD image of virtual backscatter results (similar to SEM-BSE image) overlain by the grain average image quality. Blue/green/yellow/red colors denote decreasing image quality. Gray color represents areas where no Kikuchi patterns were detected, suggesting the area is amorphous or has short-range ordering of crystals. **(B)** EBSD Kikuchi pattern from a spot in the yellow circle in panel **A**. The lattice diagram at the lower right represents the grain's crystalline structure in which the hexagonal surface is the basal plane (0001), with the c-axis perpendicular to it.

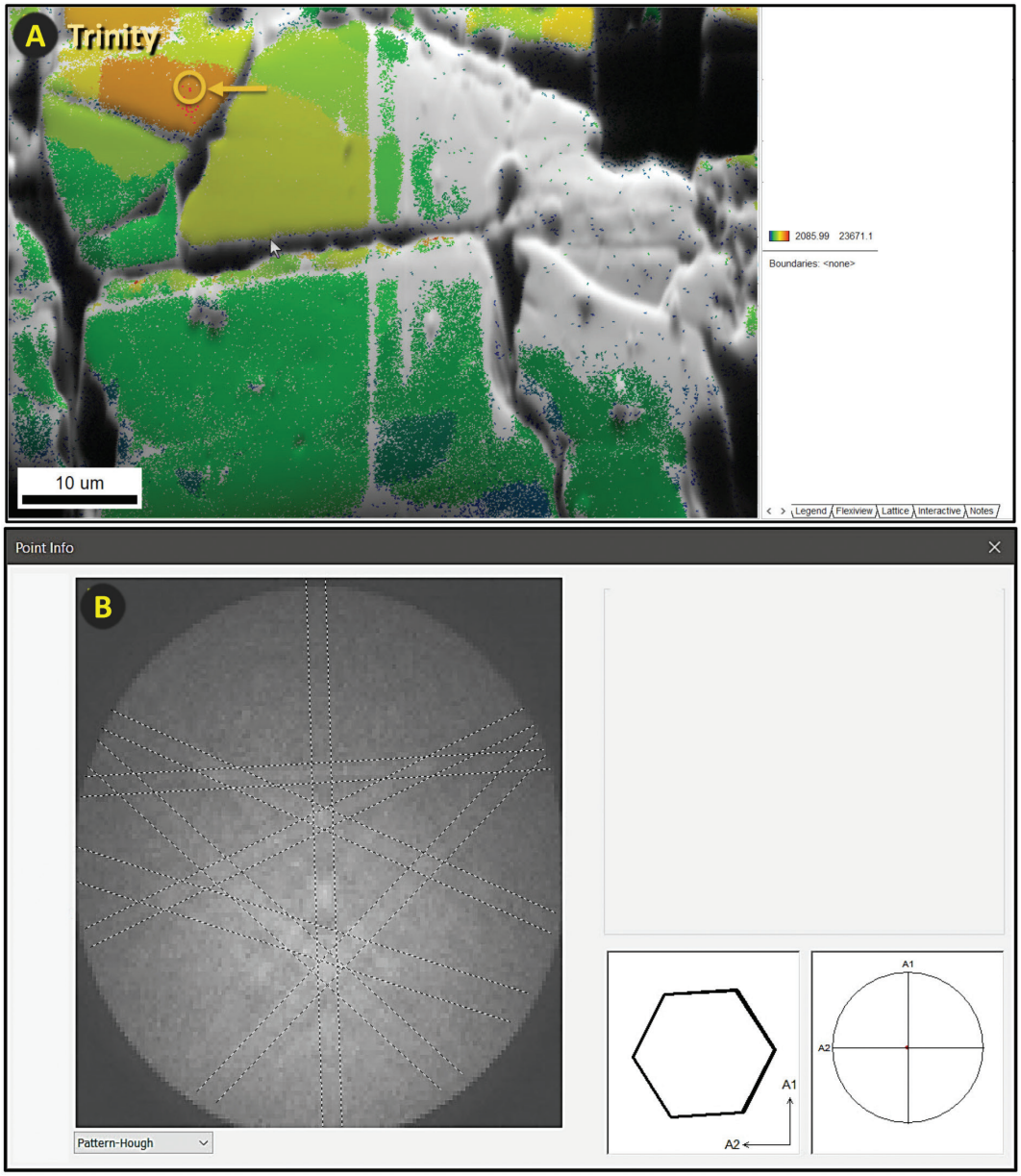

Figure S16: EBSD Kikuchi patterns of shock-fractured quartz. **(A)** Trinity meltglass grain 32x08. EBSD image of virtual backscatter results (similar to SEM-BSE image) overlain by the grain average image quality. Blue/green/yellow/red colors denote decreasing image quality. Gray color represents areas where no Kikuchi patterns were detected, suggesting the area is amorphous or has short-range ordering of crystals. **(B)** EBSD Kikuchi pattern from a spot in the yellow circle in panel **A**. The lattice diagram at the lower right represents the grain's crystalline structure in which the hexagonal surface is the basal plane (0001), with the c-axis perpendicular to it.